MNRAS **000**, 1–20 (2002) Preprint 25 November 2018 Compiled using MNRAS LATEX style file v3.0

The dynamics of stellar disks in live dark-matter halo

M. S. Fujii[1⋆], J. Bédorf[2], J. Baba[3], and S. Portegies Zwart[2]
[1]*Department of Astronomy, Graduate School of Science, The University of Tokyo, 7-3-1 Hongo, Bunkyo-ku, Tokyo, 113-0033, Japan*
[2]*Leiden Observatory, Leiden University, NL-2300RA Leiden, The Netherlands*
[3]*National Astronomical Observatory of Japan, Mitaka-shi, Tokyo 181-8588, Japan*

Accepted . Received ; in original form

ABSTRACT

Recent developments in computer hardware and software enables researchers to simulate the self-gravitating evolution of galaxies at a resolution comparable to the actual number of stars. Here we present the results of a series of such simulations. We performed N-body simulations of disk galaxies at with 100 and 500 million particles over a wide range of initial conditions. Our calculations include a live bulge, disk, and dark matter halo, each of which is represented by self-gravitating particles in the N-body code. The simulations are performed using the gravitational N-body tree-code `Bonsai` running on the Piz Daint supercomputer.

We find that the time scale over which the bar forms increase exponentially with decreasing disk-mass fraction. The effective criterion for bar formation is obtained in our simulations for a disk-to-halo mass-fractions $\gtrsim 0.25$.

These results can be explained with the swing-amplification theory. The condition for the formation of $m = 2$ spirals is consistent with that for the formation of the bar, which also is an $m = 2$ phenomenon. We further argue that the two-armed structures in grand-design spiral galaxies is a transitional phenomenon, and that these galaxies evolve to barred galaxies on a dynamical timescale. The resulting barred galaxies have rich morphology, which is also present in the Hubble sequence. We explain the sequence of spiral-galaxies in the Hubble diagram by the bulge-to-disk mass fraction, and the sequence of barred-spiral galaxies is a consequence of secular evolution.

Key words: galaxies: kinematics and dynamics — galaxies: spiral — galaxies: structure — galaxies: evolution — methods: numerical

1 INTRODUCTION

Simulations serve as a powerful tool to study the dynamical evolution of galaxies. Galaxies are extremely complicated, in particular due to the varying environmental situation and their internal evolution. Even the relatively simple self-gravity of an isolated galaxy poses an enormous challenge, because of the non-linear processes that govern the formation of spiral arms and bar-like structures. Many of these processes are attributed to external perturbations, and it is not a-priori clear to what extent internal dynamical processes play a role in the formation of axis-asymmetric structures in disk galaxies. Self-gravitating disks are prone to form spiral arms and/or bars, but the precise conditions under which these form are not well understood.

In early simulations Hohl (1971) demonstrated, using $\sim 7 \times 10^4$ cells with near-neighbour interactions, that a stellar disk without a (dark matter) halo leads to the formation of a bar within a few galactic rotations. In a subsequent study Ostriker & Peebles (1973) concluded that a dark-matter halo is required to keep the disk stable. For spiral galaxies, Sellwood & Carlberg (1984) performed simulations of two-dimensional stellar disks with ~ 7000 cells (equivalent to 2×10^4 particles) that developed multiple spiral arms. They suggested that spiral arms tend to kinematically heat-up the disk, and that in the absence of an effective coolant, such as ambient gas or star formation, this heating would cause the spiral structures to disappear within a few galactic rotations. Carlberg & Freedman (1985) also performed a series of simulations and found that the number of spiral arms decrease as the disk-to-halo mass ratio decreases. In contrast to the Lin-Shu quasi-stationary density wave theory Lin & Shu (1964), these simulations suggest that spiral arms are transient and develop from small perturbations amplified by the self-gravity in a differentially rotating disk (Goldreich & Lynden-Bell 1965; Julian & Toomre 1966). Today this mechanism is known as "swing amplification" (Toomre 1981; Michikoshi & Kokubo 2016b).

⋆ E-mail: fujii@astron.s.u-tokyo.ac.jp (MSF)

The number of particles in simulations has increased, as computers have become more powerful. After Sellwood & Carlberg (1984) and Carlberg & Freedman (1985), the formation and evolution of bar structures were often studied using thee dimensional N-body simulations. Combes et al. (1990) showed that bars induce peanut-shaped (boxy) bulge using a three-dimensional Particle-Mesh method with maximum $\sim 8\times10^6$ cells. N-body simulations with up to 2^8 particles were performed by Sellwood & Carlberg (2014), but they adopted a rigid potential for the dark matter halo.

The importance of modeling a live halo, using particles, was advertised by Athanassoula (2002). They found that once a bar formed, its angular momentum is transferred to the halo. Resolving this can only be realized if the halo is represented as a live N-body realization that is integrated together with the other particles. Such a live halo also affects the evolution of the bar. In this study, a tree method (Barnes & Hut 1986) was adopted. Several other simulations of barred galaxies, in which halos were treated as live particle distributions, were performed using a tree code (Widrow & Dubinski 2005; Widrow et al. 2008). Dubinski et al. (2009) performed a series N-body simulation of barred galaxies with a live halo using up to 10^8 particles. They confirmed that this large number of particles is sufficient to obtain a converged solution, but they also found that bar formation is delayed for larger particle numbers.

In simulations of spiral galaxies with multiple arms, Fujii et al. (2011) demonstrated that the effect of numerical heating is sufficiently small when the number of particles is sufficiently large. They argued that the disk must be resolved with at least one million particles to suppress numerical artifacts, but these simulations were performed with a rigid halo-potential. So far, it has been impossible to carry out extensive parameter searches with such numerous particles including a live halo, simply because of the amount of computer time required for such studies exceeds the hardware and software capacity (e.g. Dubinski et al. 2009). With the common availability of GPU-based supercomputers and optimized N-body algorithms, such calculations can now be realized Portegies Zwart & Bédorf (2015).

If a galactic disk needs to be resolved with at least a million particles, it is understandable that simulating an entire galaxy, including the dark matter halo, would require at least 10 times this number in order to properly resolve the disk and halo in an N-body simulation. To overcome the numerical limitations researchers tend to adopt a rigid background potential for the galaxy's dark matter halo. (e.g., Sellwood & Carlberg 1984; Fujii et al. 2011; Baba et al. 2013; Grand et al. 2013). However, this prevents the transport of energy and angular momentum from the halo to the disk, and vice versa. Taking this coupling into account is particularly important when studying the formation and evolution of non-axisymmetric structures such as spiral arms and a bar in the disk. Bars tend to slow down due to angular-moment transfer with the halo and grow faster when compared to models with a rigid halo (Debattista & Sellwood 2000; Athanassoula 2002). Until recently software and hardware were inapt to perform such high-resolution simulations. The current generation of supercomputers and the associated software allows us to perform simulations with more than a hundred billion particles (Bédorf et al. 2014) over a Hubble time, or many smaller simulations that cover a wide range of the initial conditions.

Paramount to these developments is the effective use of massively parallel supercomputers, equipped with thousands of graphical processing units (GPUs). We developed the gravitational tree-code `Bonsai` to perform such simulations. `Bonsai`, uses the GPUs to accelerate the calculations and achieves excellent efficiency with up to ~ 19000 GPUs (Bédorf et al. 2012, 2014). The efficiency of `Bonsai` allows us to run simulations with a hundred million particles for 10 Gyr in a few hours using 128 GPUs in parallel. This development allows us to perform simulations of disk galaxies for the entire lifetime of the disk, and therefore to study the formation of structure using realistic resolution and time scale, unhampered by numerical noise.

Using `Bonsai` running on the Piz Daint supercomputer we performed a large number of disk galaxy simulations with live dark-matter halos at a sufficiently high resolution to suppress numerical heating on the growth of the physical instabilities due to the self-gravity of the disk. With these simulations, we study the relation between the initial conditions and the final disk galaxies.

2 *N*-BODY SIMULATIONS

We performed a series of N-body simulations of galactic stellar disks embedded in dark matter halos. In this section, we describe our choice of parameters and the N-body code used for these simulations.

2.1 Model

Our models are based on those described in Widrow et al. (2008) and Widrow & Dubinski (2005). We generated the initial conditions using GalactICS (Widrow & Dubinski 2005). The initial conditions for generating the dark mater halo are taken from the NFW profile (Navarro et al. 1997), which has a density profile following:

$$\rho_{\rm NFW}(r) = \frac{\rho_{\rm h}}{(r/a_{\rm h})(1+r/a_{\rm h})^3}, \tag{1}$$

and the potential is written as

$$\Phi_{\rm NFW} = -\sigma_{\rm h}^2 \frac{\log(1+r/a_{\rm h})}{r/a_{\rm h}}. \tag{2}$$

Here the gravitational constant, G, is unity, $a_{\rm h}$ is the scale radius, $\rho_{\rm h} \equiv \sigma^2/4\pi a_{\rm h}^2$ is the characteristic density, and $\sigma_{\rm h}$ is the characteristic velocity dispersion. We adopt $\sigma_{\rm h} = 340$ (km s^{-1}), $a_{\rm h} = 11.5$ (kpc). Since the NFW profile is infinite in extent and mass, the distribution is truncated by a halo tidal radius using an energy cutoff $E_{\rm h} \equiv \varepsilon_{\rm h}\sigma_{\rm h}^2$, where $\varepsilon_{\rm h}$ is the truncation parameter with $0 < \varepsilon_{\rm h} < 1$. Setting $\varepsilon_{\rm h} = 0$ yields a full NFW profile (see Widrow & Dubinski 2005, for details). We choose the parameters of the dark matter halo such that the resulting rotation curves have a similar shape. The choice of parameters is summarized in Table 1.

For some models we assume the halo to have net angular momentum. This is realized by changing the sign of the angular momentum about the symmetry axis (J_z). The rotation is parameterized using $\alpha_{\rm h}$. For $\alpha_{\rm h} = 0.5$, the fraction of halo particles which have positive or negative J_z are the

same, in which case the disk has no net angular momentum. If $\alpha_h > 0.5$, the halo rotates in the same direction as the disk.

For the disk component, we adopt an exponential disk for which the surface density distribution is given by

$$\Sigma(R) = \Sigma_0 e^{-R/R_d}. \quad (3)$$

The vertical structure is given by $\mathrm{sech}^2(z/z_d)$, where z_d is the disk scale height. The radial velocity dispersion is assumed to follow $\sigma_R^2(R) = \sigma_{R0}^2 \exp(-R/R_d)$, where σ_{R0} is the radial velocity dispersion at the disk's center. Toomre's stability parameter Q (Toomre 1964; Binney & Tremaine 2008) at a reference radius (we adopt $2.2R_d$), Q_0, is controlled by the central velocity dispersion of the disk (σ_{R0}). We tune σ_{R0} such that for our standard model $Q_0 = 1.2$.

For our standard model (md1mb1), we use as disk mass M_d=4.9×10^{10} $M_\odot$, and the scale length R_d=2.8 kpc. The disk's truncation radius is set to 30 kpc, the scale height z_d=0.36 kpc and the radial velocity dispersion at the center of the galaxy to σ_{R0}=105 km s^{-1}. The disk is truncated at (R_{out}) with a radial range for disk truncation (δR). We adopt $R_{out} = 30.0$ (kpc) and $\delta R = 0.8$ (kpc).

For the bulge we use a Hernquist model (Hernquist 1990), but the distribution function is extended with an energy cutoff parameter (ε_b) to truncate the profile much in the same way as we did with the halo model. The density distribution and potential of the standard Hernquist model is

$$\rho_H = \frac{\rho_b}{(r/a_b)(1+r/a_b)^3} \quad (4)$$

and

$$\Phi_H = \frac{\sigma_b^2}{1+r/a_b}. \quad (5)$$

Here a_b, $\rho_b = \sigma_b^2/(2\pi a_b^2)$, and σ_b are the scale length, characteristic density, and the characteristic velocity of the bulge, respectively. We set σ_b=300 km s^{-1}, bulge scale length a_b=0.64 kpc, and the truncation parameter (ε_b=0.0). This results in a bulge mass of $4.6 \times 10^9 M_\odot$, which is consistent with the Milky Way model proposed by Shen et al. (2010), and reproduces the bulge velocity distribution obtained by BRAVA observations (Kunder et al. 2012). We do not assume an initial rotational velocity for the bulge.

For the simulation models we vary the disk mass, bulge mass, scale length, halo spin, and Q_0. Since the adopted generator for the galaxies is an irreversible process and due to the randomization of the selection of particle positions and velocities we cannot guarantee that the eventual velocity profile is identical to the input profile, but we confirmed by inspection that they are indistinguishable. The initial conditions for each of the models are summarized in Table 1. The mass and tidal radius for the bulge, disk, and halo as created by the initial condition generator are given in Table 2.

In each of the models we fix the number of particles used for the disk component to 8.3×10^6. For the bulge and halo particles we adopt the same particle mass as for the disk particles. As a consequence the mass ratios between the bulge, halo and disk are set by having a different number of particles used per component (Table 2).

2.2 Code: Bonsai

We adopted the `Bonsai` code for all calculations (Bédorf et al. 2012, 2014). `Bonsai` implements the classical Barnes & Hut algorithm (Barnes & Hut 1986) but then optimized for Graphics Processing Units (GPU) and massively parallel operations. In `Bonsai` all the compute work, including the tree-construction, takes place on the GPU which frees up the CPU for administrative tasks. By moving all the compute work to the GPU there is no need for expensive data copies, and we take full advantage of the large number of compute cores and high memory bandwidth that is available on the GPU. The use of GPUs allows fast simulations, but we are limited by the relatively small amount of memory on the GPU. To overcome this limitation we implemented across-GPU and across-node parallelizations which enable us to use multiple GPUs in parallel for a single simulation (Bédorf et al. 2014). Combined with the GPU acceleration, this parallelization method allows `Bonsai` to scale efficiently from single GPU systems all the way to large GPU clusters and supercomputers (Bédorf et al. 2014). We used the version of `Bonsai` that incorporates quadrupole expansion of the multipole moments and the improved Barnes & Hut opening angle criteria (Iannuzzi & Athanassoula 2013). We use a shared time-step of ~ 0.6 Myr, a gravitational softening length of 10 pc and the opening angle $\theta = 0.4$.

Our simulations contain hundreds of millions of particles and therefore it is critical that the post-processing is handled efficiently. We therefore implemented the post-processing methods directly in `Bonsai` and which is executed during while the simulation is progressing. This eliminates the need to reload a snapshot data (which are on the order of a few terabytes) after the simulation.

The simulations in this work have been run on the Piz Daint supercomputer at the Swiss National Supercomputing Centre. In this machine each compute node contains an NVIDIA Tesla K20x GPU and an Intel Xeon E5-2670 CPU. Depending on the number of particles in the simulation we used between 8 and 512 nodes per simulation.

3 RESULTS

3.1 The effects of disk and bulge masses

We study the effect that the disk and bulge mass fraction have on the halo and on the morphology of spiral arms and bars. In Fig. 1, we summarize the initial rotation curves of several models: models md1mb1, md0.5mb1, md0.3mb1, and md0.1mb1 (varying disk mass) and models md0.5mb0 and md0.5mb3 (varying bulge mass). We present the snapshots at $t = 5$ and 10 Gyr in Figs. 2 and 3. As reported in previous studies, the number of spiral arms increase as the disk mass decreases (Carlberg & Freedman 1985; Bottema 2003; Fujii et al. 2011; D'Onghia 2015) and the formation of the bar is delayed when the bulge mass is increased (Saha & Naab 2013). This corresponds to the effect that centrally concentrated potentials prevent the formation of bars (Sellwood & Evans 2001).

Table 1. Models and parameters

	Halo				Disk				Bulge		
Parameters	$a_{\rm h}$	$\sigma_{\rm h}$	$1-\varepsilon_{\rm h}$	$\alpha_{\rm h}$	$M_{\rm d}$	$R_{\rm d}$	$z_{\rm d}$	σ_{R0}	$a_{\rm b}$	$\sigma_{\rm b}$	$1-\varepsilon_{\rm b}$
Model	(kpc)	(km s^{-1})			($10^{10}M_\odot$)	(kpc)	(kpc)	(km s^{-1})	(kpc)	(km s^{-1})	
md1mb1	11.5	340	0.8	0.5	4.9	2.8	0.36	105	0.64	300	1.0
md1mb1s0.65	11.5	340	0.8	0.65	4.9	2.8	0.36	105	0.64	300	1.0
md1mb1s0.8	11.5	340	0.8	0.8	4.9	2.8	0.36	105	0.64	300	1.0
md0.5mb1	8.2	310	0.88	0.5	2.5	2.8	0.36	59.2	0.64	300	0.86
md0.4mb1	7.6	300	0.91	0.5	2.0	2.8	0.36	49.0	0.64	300	0.84
md0.3mb1	7.0	287	0.92	0.5	1.5	2.8	0.36	38.5	0.64	300	0.82
md0.1mb1	6.0	285	0.97	0.5	0.49	2.8	0.36	13.5	0.64	300	0.79
md0.5mb0	22.0	450	0.7	0.5	2.3	2.8	0.36	62.6	0.64	500	0.86
md0.5mb3	7.0	270	0.8	0.5	2.3	2.8	0.36	59.0	0.64	500	0.79
md0.5mb4	6.6	260	0.82	0.5	2.3	2.8	0.36	58.3	0.64	545	0.80
md0.5mb4rb3	13.5	360	0.8	0.5	2.3	2.8	0.36	57.2	1.92	380	0.99
md1mb1Rd1.5	9.0	290	0.95	0.5	4.9	4.2	0.36	74.2	0.64	300	0.85
md0.5mb1Rd1.5	7.5	290	0.91	0.5	2.5	4.2	0.36	39.8	0.64	300	0.8
md0.5Rmb1d1.5s	7.5	290	0.91	0.8	2.5	4.2	0.36	39.8	0.64	300	0.8
md1.5mb5	13.0	280	0.9	0.5	7.3	2.8	0.36	138	1.0	550	0.8
md1mb10	18.0	500	0.9	0.5	4.9	2.8	0.36	93.2	1.5	600	1.0
md0.5mb0Q0.5	22.0	450	0.7	0.5	2.3	2.8	0.36	26.1	0.64	500	0.86
md0.5mb0Q2.0	22.0	450	0.7	0.5	2.3	2.8	0.36	105	0.64	500	0.86

Table 2. Models: mass, radius, and number of particles per component

Model	$M_{\rm d}$ ($10^{10}M_\odot$)	$M_{\rm b}$ ($10^{10}M_\odot$)	$M_{\rm h}$ ($10^{10}M_\odot$)	$R_{\rm d,t}$ (kpc)	$r_{\rm b,t}$ (kpc)	$r_{\rm h,t}$ (kpc)	Q_0	$M_{\rm b}/M_{\rm d}$	$N_{\rm d}$	$N_{\rm b}$	$N_{\rm h}$
md1mb1	4.97	0.462	59.7	31.6	3.17	229	1.2	0.0930	8.3M	0.77M	100M
md1mb1s0.65	4.97	0.462	59.7	31.6	3.17	229	1.2	0.0930	8.3 M	0.77M	100M
md1mb1s0.8	4.97	0.462	59.7	31.6	3.17	229	1.2	0.0930	8.3M	0.77M	100M
md0.5mb1	2.55	0.465	43.8	31.6	2.56	232 1.2		0.182	8.3M	1.5M	140M
md0.4mb1	2.05	0.463	41.4	31.6	2.52	261	1.2	0.226	8.3M	1.9M	170M
md0.3mb1	1.56	0.462	36.2	31.6	2.49	247	1.2	0.296	8.3M	2.5M	190M
md0.1mb1	0.546	0.466	33.3	31.6	2.44	340	1.2	0.853	8.3M	7.1M	510M
md0.5mb0	2.53	0.0	100.0	31.6	-	295	1.2	0.00	8.3M	-	330M
md0.5mb3	2.61	1.37	39.7	31.6	2.81	120	1.2	0.525	8.3M	4.4M	130M
md0.5mb4	2.62	1.69	41.4	31.6	2.96	125	1.2	0.645	8.3M	5.4M	130M
md0.5mb4rb3	2.60	1.76	86.7	31.6	8.55	229	1.2	0.676	8.3M	5.4M	130M
md1mb1Rd1.5	5.06	0.464	47.1	46.6	2.61	620	1.2	0.0916	8.3M	0.77M	78M
md0.5mb1Rd1.5	2.59	0.457	35.2	46.6	2.47	249	1.2	0.176	8.3M	1.5M	110M
md0.5mb1Rd1.5s	2.59	0.457	35.2	46.6	2.47	249	1.2	0.176	8.3M	1.5M	110M
md1.5mb5	7.52	2.09	104.6	31.6	3.53	269	1.2	0.279	8.3M	2.3M	120M
md1mb10	5.17	5.22	2050	31.6	11.6	264	1.2	1.0	8.3M	8.4M	400M
md0.5mb1Q0.5	2.55	0.465	43.8	31.6	2.56	232	0.5	0.182	8.3M	1.5M	140M
md0.5mb1Q2.0	2.55	0.465	43.8	31.6	2.56	232	2.0	0.182	8.3M	1.5M	140M

Column 1: Model name, 2: Disk mass, 3: Bulge mass, 4: Halo mass, 5: disk outer radius, 6: bulge outer radius, 7: Halo outer radius, 8: Toomre's Q value at the reference point ($2.5R_{\rm d}$), 9: Bulge-to-disk mass ratio (B/D), 10: Number of particles for the disk, 11: Number of particles for the bulge, 12: Number of particles for the halo.

Table 3. Bar formation

Model	Bar formation	Bar formation epoch t_b (Gyr)	Bar formation criteria ε_m	X_{min}	$X'(\equiv 1/f_d)$
md1mb1	Y	0.64	0.824	0.997	1.80
md1mb1s0.65	Y	0.83	0.824	0.997	1.80
md1mb1s0.8	Y	0.73	0.824	0.997	1.80
md0.5mb1	Y	6.3	1.03	1.68	2.61
md0.4mb1	Y	13	1.00	1.97	2.96
md0.3mb1	Y	18	1.87	2.41	3.49
md0.1mb1	N	-	2.12	5.78	8.34
md0.5mb0	Y	3.1	1.08	0.827	2.28
md0.5mb3	Y	7.0	1.26	2.17	2.88
md0.5mb4	Y	9.9	1.38	2.58	3.06
md0.5mb4rb3	Y	9.9	1.15	2.80	3.17
md1.5mb5	Y	1.9	1.42	1.30	1.69
md1mb10	Y	7.5	1.60	2.71	2.86
md1mb1Rd1.5	Y	2.6	0.960	1.41	2.38
md0.5mb1Rd1.5	N	-	1.25	2.35	3.77
md0.5mb1Rd1.5s	N	-	1.25	2.35	3.77
md0.5mb1Q0.5	Y	0.27	1.03	1.68	2.61
md0.5mb1Q2	Y	8.8	1.03	1.68	2.61

Bar formation: Yes (Y) or No (N) within the simulation time period (0–20 Gyr)

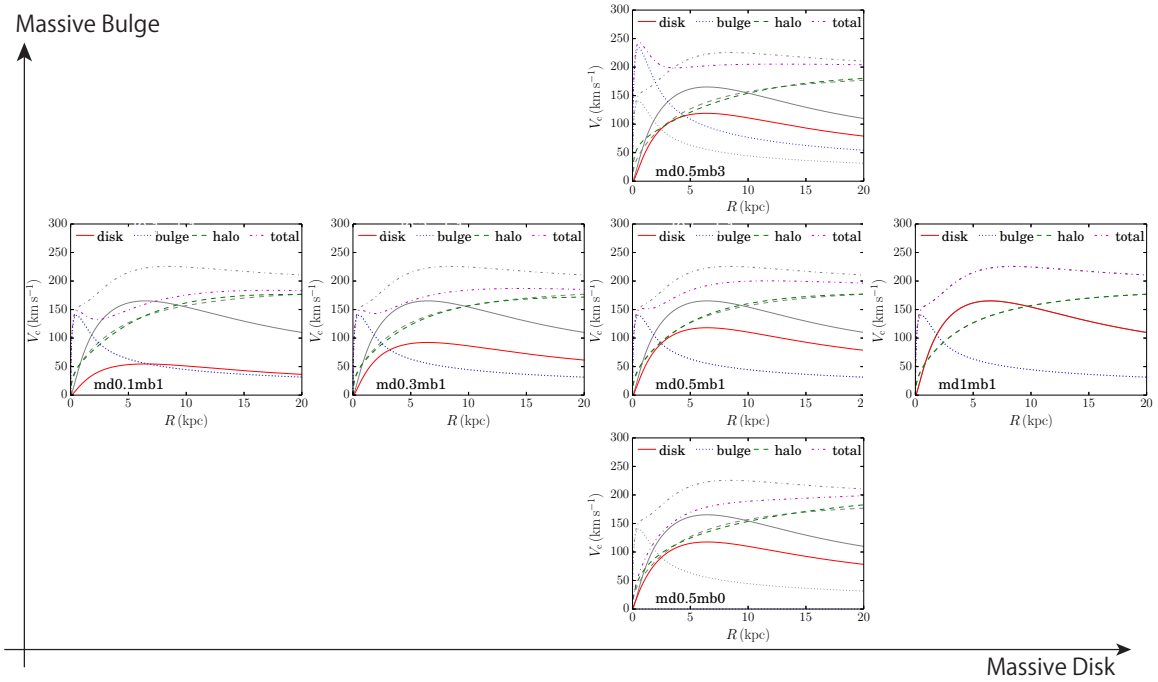

Figure 1. Rotation curves of the initial conditions for models md1mb1, md0.5mb1, md0.3mb1, md0.1mb1, md0.5mb0, and md0.5mb3.

3.2 Number of Spiral Arms

We first focus on the number of spiral arms. As is shown in Fig. 3, the number of spiral arms increases as the disk mass decreases. This relation can be understood by swing amplification theory (Toomre 1981). In a differentially rotating disk, the epicycle motions of particles are amplified and the amplification factor X is written as

$$X \equiv \frac{k_{crit} R}{m} = \frac{\kappa^2 R}{2\pi G \Sigma m}. \quad (6)$$

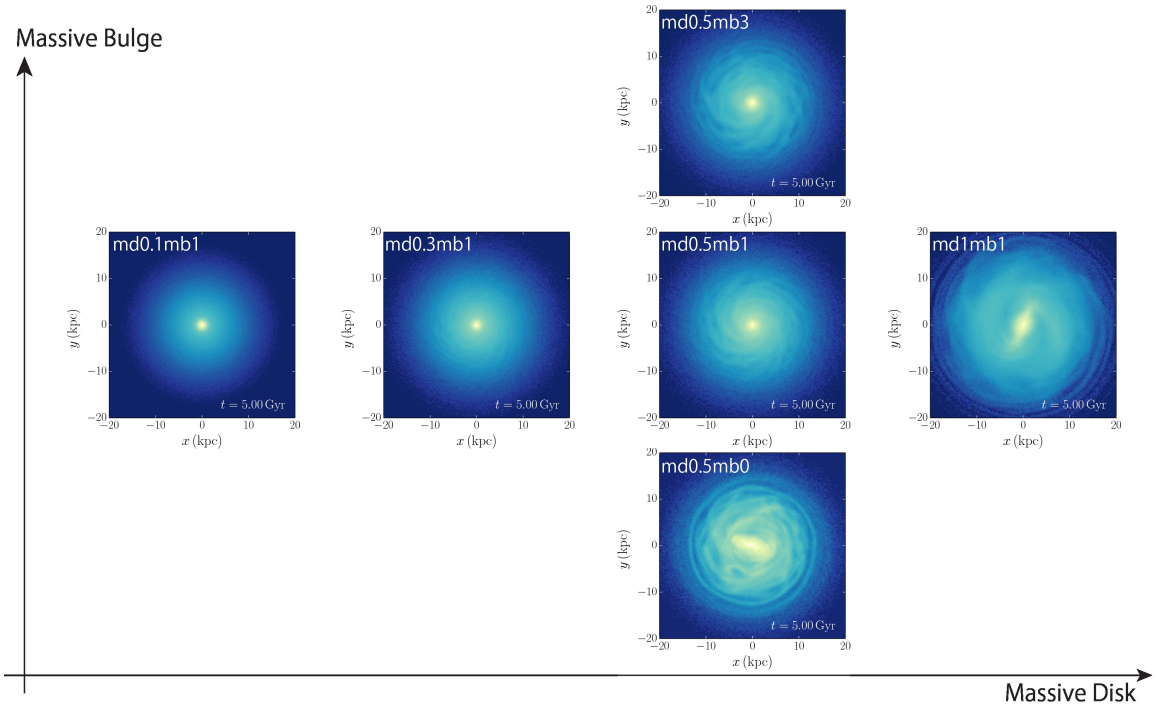

Figure 2. Snapshots (surface densities) at $t = 5$ Gyr for models md1mb1, md0.5mb1, md0.3mb1, md0.1mb1, md0.5mb0, and md0.5mb3.

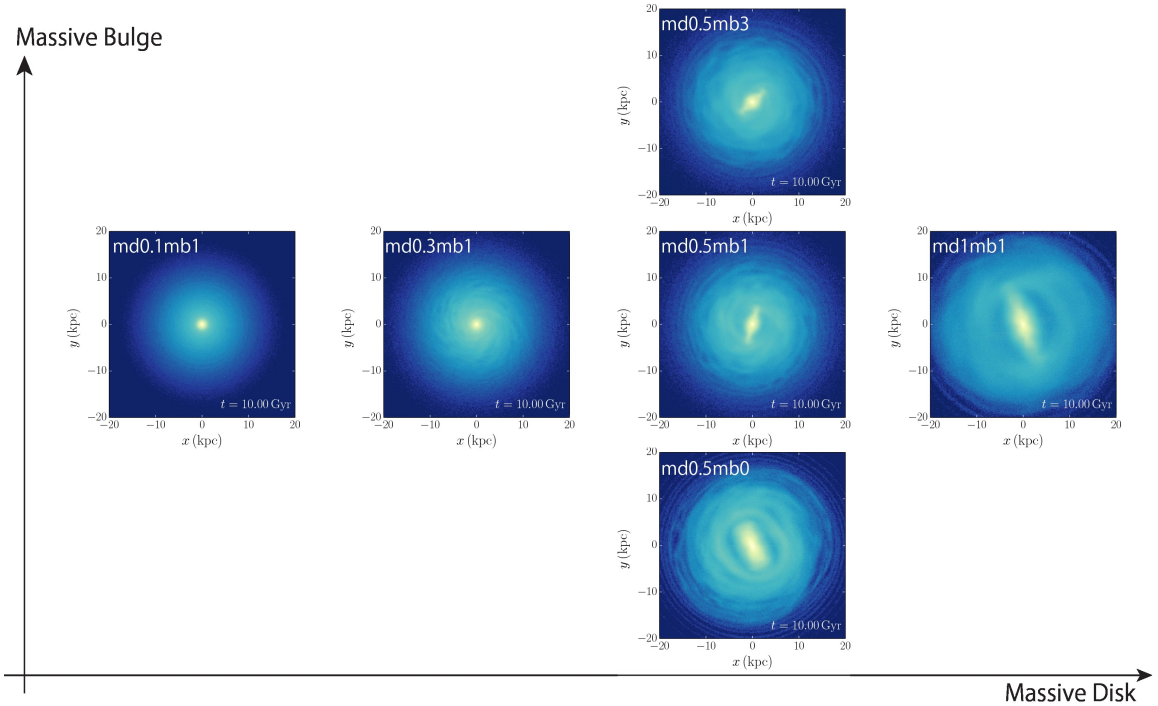

Figure 3. Snapshots (surface densities) at $t = 10$ Gyr for models md1mb1, md0.5mb1, md0.3mb1, md0.1mb1, md0.5mb0, and md0.5mb3.

Here R is the distance from the center of the galactic and m is the number of the mode (a bar or the number of spiral arms). For typical disk models the amplification is large for $1 \lesssim X \lesssim 2$ and rapidly drops for $2 \lesssim X \lesssim 3$ (Goldreich & Lynden-Bell 1965; Julian & Toomre 1966; Toomre 1981). The critical wave number $k_{\rm crit}$ (and also the critical wave length $\lambda_{\rm crit}$) is obtained from the local stability in a razor-thin disk using

the tight-winding approximation (Toomre 1964):

$$k_{\rm crit} = \frac{\kappa^2}{2\pi G\Sigma}, \quad (7)$$

$$\lambda_{\rm crit} = \frac{2\pi}{k_{\rm crit}} = \frac{4\pi^2 G\Sigma}{\kappa^2}, \quad (8)$$

where Σ and κ are the surface density and the epicyclic frequency of the disk, respectively (see also section 6.2.3 of Binney & Tremaine 2008).

Equation (6) also predicts the number of spiral arms that form in a disk. By inverting equation (6) one obtains a relation for the mode as a function of the swing amplification factor X:

$$m = \frac{\kappa^2 R}{2\pi G\Sigma X}. \quad (9)$$

Because the perturbations grow most efficiently for $X \sim 1$–2, we can relate m as a function of R (here, both κ and Σ are written as a function of R.). The predicted number of spiral arms from swing amplification theory has been validated using numerical simulations (Carlberg & Freedman 1985; D'Onghia 2015).

For models with different disk masses, we estimate the number of spiral arms using equation (9) and present the results in Fig. 4. The dashed curves present the estimated number of spiral arms as a function of galactic radii where we adopt $X \sim 2$ following Carlberg & Freedman (1985); Dobbs & Baba (2014). Given the curves we expect fewer arms for the more massive models and the number of arms increases for larger radii (R).

We also determine the number of spiral arms for each of the simulated galaxies and overplot the results in Fig. 4. We use a Fourier decomposition of the disks surface density:

$$\frac{\Sigma(R,\phi)}{\Sigma_0(R)} = \sum_{m=0}^{\infty} A_m(R) e^{im[\phi-\phi_m(R)]}, \quad (10)$$

where $A_m(R)$ and $\phi_m(R)$ are the Fourier amplitude and phase angle for the m-th mode at R, respectively. We measure the amplitude at each radius up to 20 kpc using radial bins of $\Delta R = 1$ kpc.

Because the spiral arms are transient structures the dominant number of spiral arms, those with the highest amplitude, changes over time (Fujii et al. 2011). We therefore use the most frequently appearing number of spiral arms (hereafter, principle mode) as the number of arms (m) of the model. The principle mode is measured between 2.5 and 14.5 kpc at 2 kpc intervals, and for each the 1000 snapshots between 0 and 10 Gyr. The results are presented in Fig. 4. The $m = 2$ mode will always become the dominant mode once a bar has formed (see red circles in the figure), but spiral arms might have formed before the bar formation. We therefore also show the principle mode before the bar formation (triangular symbols). These results are consistent with the number of spiral arms predicted by Eq. 9. For model md0.1mb1 we measure a principle mode of 2 at R =6.5 kpc. However, when we look at Fig. 3, we see faint spiral arms more than 2. We therefore also measured the strongest modes excluding $m = 2$. These modes are indicated by the square symbols. We perform the same analysis for all the other models and measure the number of spiral arms (for the details of the individual evolution of these models, see the following sections and Appendix B). The results are summarized in Table 4

In Fig. 4 we demonstrated how the numbers of spiral arms change with galactic radius. The number of spiral arms and the mass fraction of the disk are typically measured at $2.2R_{\rm d}$. The relation between the measured number of spiral arms (m) at $2.2R_{\rm d}$ and the disk mass fraction ($f_{\rm d}$) is presented in Fig. 5 where ($f_{\rm d}$) is defined as:

$$f_{\rm d} \equiv \left(\frac{V_{\rm c,d}(R)}{V_{\rm c,tot}(R)}\right)^2_{R=2.2R_{\rm d}}, \quad (11)$$

where $V_{\rm c,d}$ and $V_{\rm c,tot}$ are the circular velocity of the disk and of the whole galaxy, respectively. We find that m, before the bar formation, decreases as $f_{\rm d}$ increases. This matches the results of D'Onghia (2015) (their figure 3). We further find that that models with a large bulge-to-disk mass ratio (B/D) tend to have fewer spiral arms than models with the same $f_{\rm d}$ (see red circles in Fig. 5).

We next investigate the effect of the bulge mass. A massive central component, such as a bulge, can stabilize the disk and prevent bar formation (Saha & Naab 2013). To test this we perform a set of simulations in which we change the bulge mass. We make the bulge 0 (md0.5mb0), 3 (md0.5mb3) and 4 (mb0.5mb4) times as massive as md0.5mb1. We further added model md0.5mb4rb3 which is the same as md0.5mb4 but in which we increased the scale length of the bulge. The evolution of the amplitude and length of the bar in these models is presented in Fig. 6. The bar forms later for increasing bulge mass-fraction because the disk mass fraction ($f_{\rm d}$) decreases for increasing bulge mass-fraction (also see Table 3). These results are consistent with observations that the fraction of barred galaxies increases when the bulge light to fraction decreases and that in the extreme of a bulge-less galaxy the fraction of barred galaxies is $\sim 87\%$ (Barazza et al. 2008).

3.3 Bar Formation

We will now investigate the formation of bars. In order to define the bar formation, we measure the time evolution of the length (radius) of the bar and its amplitude which develops in our galaxy simulations. Because this has to be done for one thousand snapshots for each galaxy simulation we adopt a relatively simple method for measuring these properties. We measure the Fourier amplitude (Eq. 10) in radial bins of 1 kpc for the $m = 2$ mode ($A_2(R)$), record the maximum value and use this as the bar amplitude ($A_{2,\rm max}$). In the left panel of Fig. 7, we present the time evolution of $A_{2,\rm max}$ for models md1mb1 to md0.1mb1. Once a bar begins to develop the amplitude increases exponentially and either reaches a stable maximum (as is the case in model md1mb1) or decreases slightly to increase again a few Gyr later (see model mb0.5mb1). Model md0.1mb1 did not form a bar within 10 Gyr. We also measure the bar length using the method described in Scannapieco & Athanassoula (2012) and Okamoto et al. (2015). In this method compute the phase angle ($\phi_2(R)$) and amplitude ($A_2(R)$) of the bar at each radius using the Fourier analysis (Eq. 10). As R increases, $A_2(R)$ increases, reaches its maximum in the middle of the bar, and then decreases. We define the radius at which $A_2(R)$ reaches its maximum value as $R_{\rm max}$ and the phase at $R_{\rm max}$ as the phase angle of the bar ($\phi_{2,\rm max}$). Starting at $R_{\rm max}$, we compare $\phi_2(R)$ with $\phi_{2,\rm max}$. When $\Delta\phi = |\phi_2(R) - \phi_{2,\rm max}| > 0.05\pi$,

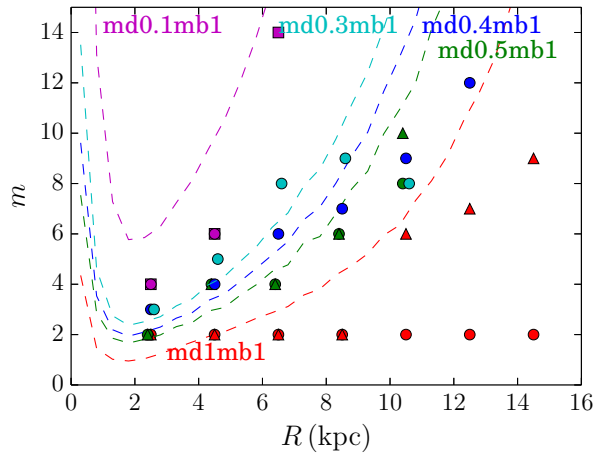

Figure 4. Theoretically predicted (using Eq. 9, dashed curves) and measured number of spiral arms (symbols) for models md0.1mb1 (magenta), md0.3mb1 (cyan), md0.4mb1 (blue), md0.5mb1 (green), and md1mb1 (red) from top to bottom. Filled circles indicate the most frequently appearing number of arms (principle modes) over a 10 Gyr period. Triangle symbols indicates the principle mode before the formation of the bar. Square symbols indicate the principle mode for model md0.1mb1 excluding $m = 2$. The symbols for md0.3mb1 and md0.5mb1 are shifted by 0.1 kpc to avoid overlapping points .

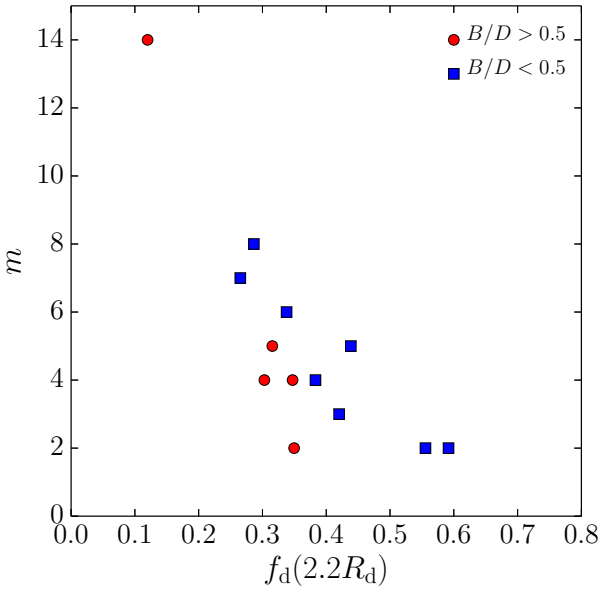

Figure 5. The measured number of spiral arms (m) before the bar formation epoch. The disk mass fraction is ($f_{\rm d} = V_{\rm c,d}(R)^2/V_{\rm c,tot}(R)^2{}_{R=2.2R_{\rm d}}$) for the models with $Q_0 = 1.2$ and without halo spin. We measure m at 6.5 kpc, which is close to $2.2R_{\rm d}$, for all models except md1mb1Rd1.5 and md0.5mb1Rd1.5. For these we measure m at 9.5 kpc. Blue squares (red circles) indicate models with a bulge-to-disk mass ratio (B/D) that is larger (smaller) than 0.5.

we consider that the bar has ended and define the radius as the bar length, ($D_{\rm b}$). The time evolution of the bar length is presented in the right panel of Fig. 7. The length of the bar grows continuously until the end of simulation ($t = 15$ Gyr).

We define the epoch of bar formation ($t_{\rm b}$) as the moment when $A_{2,\rm max} > 0.2$ and $D_{\rm b} > 1$ kpc. In our models the bar was always longer than 1 kpc when $A_{2,\rm max} > 0.2$. In most cases the bar amplitude increases exponentially and therefore the critical amplitude has little effect on the moment the bar forms. For models md0.4mb1 and md0.3mb1, which did not form a bar within 10 Gyr, we continued the simulations until a bar formed after 13 and 18 Gyr, respectively (also see Fig. 7 and Table 3). We continued the simulations up to 15 Gyr for md0.5mb4 and md0.5mb4rb3 to confirm that they form a bar, which they do around $\sim$ 10Gyr. The bar formation epoch for all models is presented in Table 3.

In Fig. 8, we present the relation between the bar formation epoch and the disk mass fraction, $f_{\rm d}(= 1/X')$, where X' is a parameter adopted by Widrow et al. (2008) as a bar

Table 4. Pitch angle and number of spiral arms

Model	Radius (R) (kpc)	Shear rate (Γ)	Pitch angle (i) (degree)	Maximum amplitude	Number of arms (m)
md1mb1	10	0.991	18	0.198	2
	12	1.04	18	0.164	2
	14	1.07	19	0.161	2
md1mb1s0.8	8	0.902	18	0.261	2
	10	0.991	19	0.169	2
	12	1.04	18	0.181	2
	14	1.07	22	0.197	2
md0.5mb1	6	0.804	25	0.101	4
	8	0.875	25	0.121	6
	10	0.944	27	0.0836	7
	12	0.983	18	0.0561	2
md0.4mb1	4	0.758	33	0.0372	5
	6	0.796	33	0.0442	6
	8	0.863	27	0.0378	7
	10	0.926	26	0.0249	9
md0.3mb1	4	0.774	32	0.0483	4
	6	0.792	34	0.0453	7
	8	0.847	26	0.0347	9
	10	0.907	29	0.0189	10
md0.1mb1	6	0.744	5	0.00965	1
	8	0.777	3	0.0116	1
	10	0.832	3	0.0111	2
	12	0.885	3	0.0107	2
md0.5mb0	8	0.833	15	0.185	2
	10	0.888	11	0.169	2
	12	0.905	12	0.199	2
md0.5mb3	6	0.991	25	0.131	2
	8	0.955	25	0.119	5
	10	0.963	22	0.0959	3
md0.5mb4	6	0.975	25	0.111	4
	8	0.977	23	0.109	4
	10	0.996	25	1.064	8
md0.5mb4rb3	6	0.963	26	0.0924	5
	8	0.961	25	0.0923	5
	10	0.965	26	0.0725	5
md1.5mb5	8	1.01	21	0.281	2
	10	1.07	16	0.189	2
	12	1.09	14	0.212	2
	14	1.13	11	0.269	2
md1mb10	6	1.10	27	0.287	2
	8	1.07	22	0.269	2
	10	1.05	18	0.211	2
md1mb1Rd1.5	10	0.878	24	0.152	4
	12	0.963	28	0.169	4
	14	1.03	18	0.181	4
md0.5mb1Rd1.5	10	0.850	29	0.0777	7
	12	0.921	27	0.0671	8
	14	0.977	24	0.0572	8
md0.5mb1Rd1.5s	10	0.850	26	0.0719	7
	12	0.921	26	0.0804	7
	14	0.977	24	0.0553	8

formation criterion:

$$X' \equiv 1/f_{\rm d} = \left(\frac{V_{\rm c,tot}(R)}{V_{\rm c,d}(R)}\right)^2_{R=2.2R_{\rm d}}. \quad (12)$$

They argued that $X' \lesssim 3$ (for $f_{\rm d} \gtrsim 0.3$) is the bar formation criterion in their simulation. The epoch of bar formation increases exponentially for decreasing disk mass-fraction, although the scatter is large. We fit an exponential function to our results obtained with $N_{\rm d} = 8$M and $Q_0 = 1.2$ and find that $t_{\rm b} = 0.146 \pm 0.079 \exp(1.38 \pm 0.17/f_{\rm d})$. The result is indicated by the dashed black line in Fig. 8.

The resolution of the simulation in the number of particles is an important source for the scatter (Dubinski et al. 2009); a smaller number of particles for the same model results in faster bar formation. We confirm this by performing simulations with an order of magnitude lower resolution

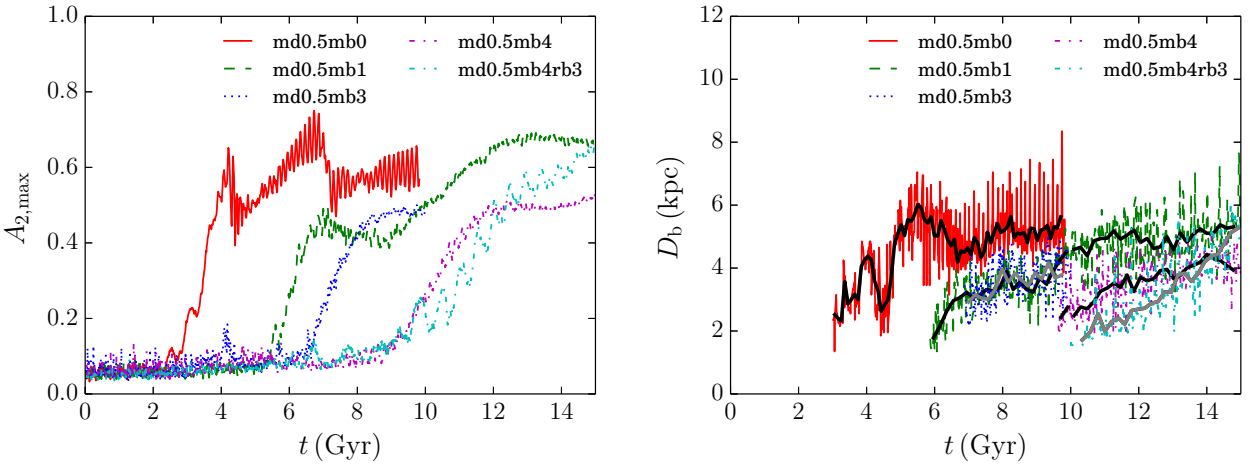

Figure 6. Time evolution of the maximum amplitude for $m = 2$ (left) and the bar length (right) for models md0.5mb0, md0.5mb1, md0.5mb3, md0.5mb4, and md0.4mb4rb3. Black curves in the right panel indicate the bar length averaged over every 20 snapshots (~ 0.2Gyr).

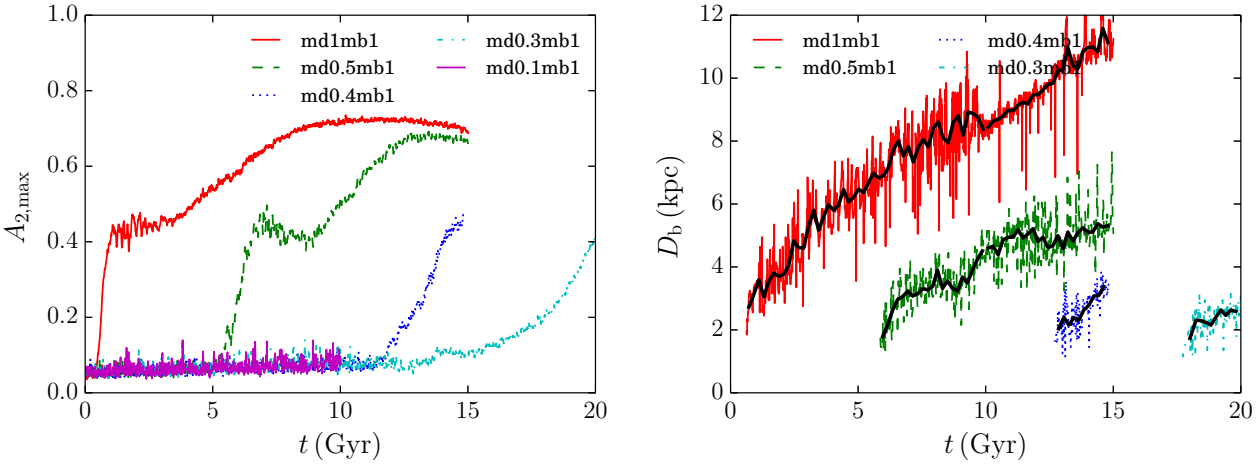

Figure 7. Same as Fig. 6 but for models md0.1mb1, md0.3mb1, md0.4mb1, md0.5mb1, and md1mb1.

(0.8 M disk particles, open circle symbols), and indeed find that the bar forms earlier for these models in comparison with the high resolution models (Fig. 8, Table 3). Another parameter which is known to affect the epoch of bar formation is the value of Q. In Fig. 8 we also plot models md0.5mb1Q2.0 and md0.5mb1Q0.5, which are identical to model md0.5mb1, with the exception that $Q_0 = 2.0$ and 0.5, respectively. In Fig. 8 we demonstrate that a larger value of Q_0 causes a delay in the formation of the bar (see Appendix A2 for the details).

The relation between the moment of bar formation ($t_{\rm b}$) and the mass fraction of the disk ($f_{\rm d}$) can be understood from Toomre's X parameter (see Eq. 6). For a given value of m we can calculate X as a function of the disk radius R. When we adopt $m = 2$, i.e. the bar, we obtain X for the bar mode (X_2) as a function of R. This distribution is presented in Fig. 9. Here, we see that X_2 reaches minimum values at $R \sim 2$ kpc. We find that the minimum value of X_2 ($X_{\rm min}$) is roughly correlated with $X'(= 1/f_{\rm d})$, and the relation between $X_{\rm min}$ and X' is presented in Fig. 10. Thus, the disk fraction $f_{\rm d}$ is connected to Toomre's X. As shown by Toomre (1981), the amplitude grows most efficiently for $1 < X < 2$ and decreases exponentially when X increases from ~ 2 to ~ 3. We find that models in which a bar forms have a minimum value of $X_2 \lesssim 2$ (see Fig. 9). We conclude, based on these results, that there is no particular rigid criterion for bar formation, but that bars start to grow exponentially when $f_{\rm d} \gtrsim 0.3$, or equivalently if $X' \lesssim 0.3$.

We also test the bar formation criterion previously suggested by Efstathiou et al. (1982), who proposed that bar formation depends on the mass of the disk ($M_{\rm d}$) within radius $R_{\rm d}$:

$$\varepsilon_{\rm m} \equiv \frac{V_{\rm c,max}}{(GM_{\rm d}/R_{\rm d})^{1/2}} < 1.1. \quad (13)$$

Here $V_{\rm c,max}$ is the maximum circular velocity in the disk. In Table 3, we present $\varepsilon_{\rm m}$ (Eq. 13), but we find that in our simulations Efstathiou's criterion cannot always predict the bar formation.

For model md0.4mb4rb3 we increased the scale length of the bulge with respect to that of model md0.4mb4 in order to see the effect of the bulge scale length. When we compare

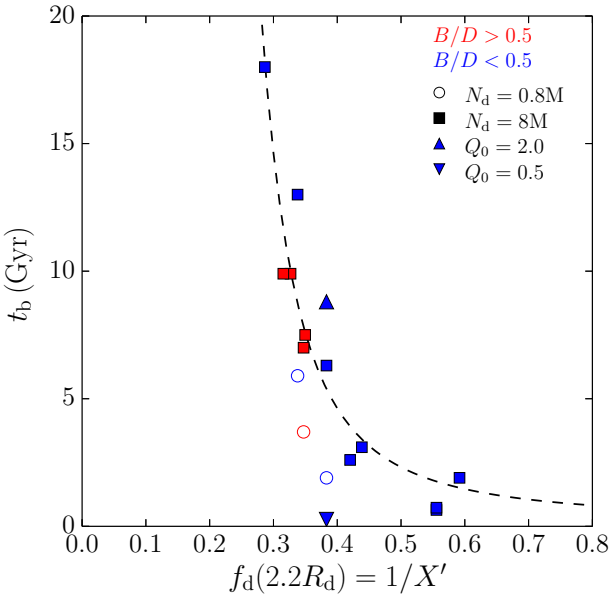

Figure 8. Bar formation epoch ($t_{\rm b}$) and disk mass fraction ($f_{\rm d} = 1/X'$). Filled squares and open circles indicate models with $N_{\rm d} = 8$M and 0.8M, respectively. Red (blue) indicates models with a bulge-to-disk ratio (B/D) of > 0.5 (< 0.5). The dashed curve indicates a fit to the models with $N_{\rm d} = 8$M and $Q_0 = 1.2$ (squares): $t_{\rm b} = 0.146 \pm 0.079 \exp(1.38 \pm 0.17/f_{\rm d})$.

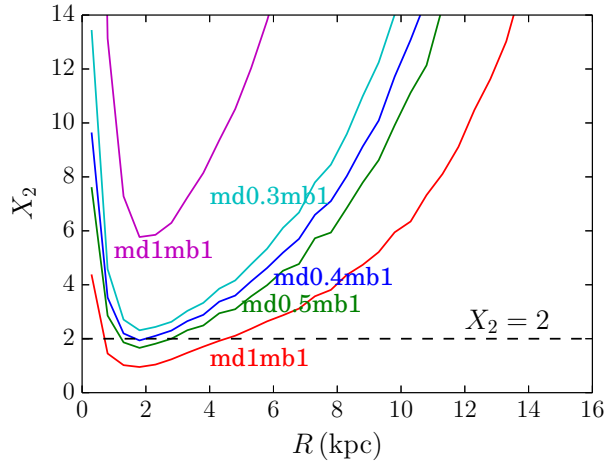

Figure 9. X values as a function of radius for $m = 2$ mode.

the results of these models, we see no indication that this effects the bar formation epoch. However, the bar length at the end of the simulation (at 15 Gyr) is longer for model md0.4mb4rb3 than that of md0.4mb4.

3.4 Pitch angle

The pitch angle is an important parameter in the discussion on the morphology of spiral galaxies. We measure the pitch angle of our simulated galaxies using the Fourier transform method (see Grand et al. 2013; Baba 2015). Using the same Fourier decomposition (Eq. 10) as for the bar amplitude we compute the phase angle, $\phi_m(R)$. Next, the pitch angle at R for m is obtained by using

$$\cot i_m(R) = R \frac{d\phi(R)_m}{dR}. \quad (14)$$

In numerical simulations the pitch angle changes over time (Baba et al. 2013; Grand et al. 2013; Baba 2015). The pitch angles of spiral arms increase and decrease repeatedly as the amplitude of transient spiral arms increases and decreases (see Figures 4 and 5 in Baba 2015). Furthermore, the number of spiral arms also changes as a function of R as we see in previous sections. We therefore measure the most appearing pitch angle for the most appearing mode (principal mode) at each galactic radius. Following Baba (2015), we define the most frequently appearing pitch angle weighted by the Fourier amplitude as the pitch angle. In Table 4, we report the measured pitch angle and the number

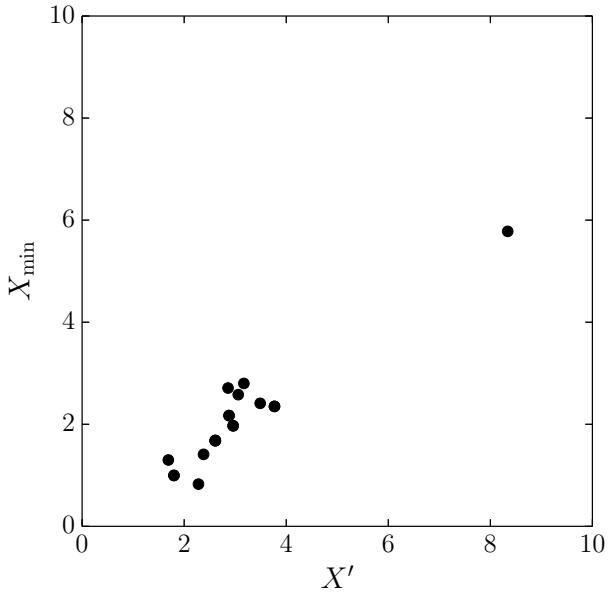

Figure 10. Relation between X' and the minimum value of X ($X_{\rm min}$).

of spiral arms (m) for the angle. Note that we measure pitch angles at $\gtrsim 2.2R_{\rm d}$, but for barred galaxies we adopt larger R than the maximum bar length to avoid the influence of the bar.

Julian & Toomre (1966) suggested that the pitch angle is determined by the shear rate of the disk. The relation between the shear rate (Γ) and pitch angle was recently investigated using both numerical simulations and analytic models (Michikoshi & Kokubo 2014, 2016a). The relation is also suggested by observations of galaxies (Seigar 2005; Seigar et al. 2006). We therefore measured the shear rates of our simulated galaxies and the results are also summarized in Table 4. The shear rate in our study is defined as

$$\Gamma = -d\ln\Omega/d\ln R, \tag{15}$$

where Ω is angular velocity.

In Fig. 11, we present the relation between the shear rate (Γ) and the measured pitch angles (i) averaged for each model. In order to compare our results with the theory, we also present the relation between shear rate and pitch angle as derived by (Michikoshi & Kokubo 2014):

$$\tan i = \frac{7}{2}\frac{\sqrt{4-2\Gamma}}{\Gamma}. \tag{16}$$

In the figure this relation is presented with a dashed curve. Except for two extreme models (md0.5mb0 and md0.1mb1), the measured relation in our simulations is consistent with the theoretical curve. Model md0.5mb0 has a strong bar due to the lack of the bulge, which results in a ring structure around the bar (see Fig. 3). For md0.1mb1 the disk is relatively light and the spirals are very faint (see Fig. 3). This morphology is similar to flocculent galaxies. We also present the relation between the shear rate and the pitch angles of observed galaxies (Seigar et al. 2006) in Fig. 11 (black points). These points are also distributed around the theoretical curve with a scatter larger than the simulated galaxies.

3.5 Bulge-to-Disk ratio

From an observational perspective such as in the Hubble sequence (Hubble 1926), the bulge-to-disk ratio (B/D) is related to the pitch angle. Sa galaxies have a larger bulge-to-disk mass-ratio compared to Sb and Sc galaxies (Kormendy & Norman 1979). To test this hypothesis we perform extra simulations (model md1mb10) which represent S0/Sa galaxies that have a massive bulge compared to the disk. The disk-to-halo mass ratio of this model is relatively large ($B/D = 1.0$), but the disk-to-total mass ratio ($f_{\rm d} = 0.35$) is not as large as for models which form a bar before forming spiral arms. The S0–Sa galaxies, for example, NGC 1167 (Zasov et al. 2008) and M 104 (Tempel & Tenjes 2006), have a such a massive bulge and also many narrow spiral arms.

In Fig. 12 we present the rotation curves (left panel) and the surface-density images (right panels) for model md1mb10. This model formed multiple spiral arms similar to Sa galaxies before it developed a bar. The measured pitch angle was $\sim 20^\circ$ within 10 kpc but less than 10° at $R > 10$ kpc.

In the previous subsection, we demonstrated the relation between the pitch angle and the shear rate (Γ). Here, in Fig. 13, we present the relation between the shear rate and bulge-to-disk mass ratio (B/D). For most of our models, Γ is correlated with B/D, but the models with a small $f_{\rm d}$ tend to have a small Γ. This is because the shear rate depends on the spherical component fraction in relation to the disk, but the spherical component does not necessarily have to be a bulge. Thus, galaxies with a massive bulge tend to form tightly-wound spirals, but the shear rate (Γ) is more essential to the pitch angle than B/D.

In addition, we look at the relation between B/D and the bar formation epoch ($t_{\rm b}$). We present this using the red symbols for models with $B/D > 0.5$ in Fig. 8. Models with a large B/D tend to take a shorter time before the bar formation, but compared to the dependence on $f_{\rm d}$, the effect of B/D on $t_{\rm b}$ is unclear. Thus, we conclude that the disk-to-

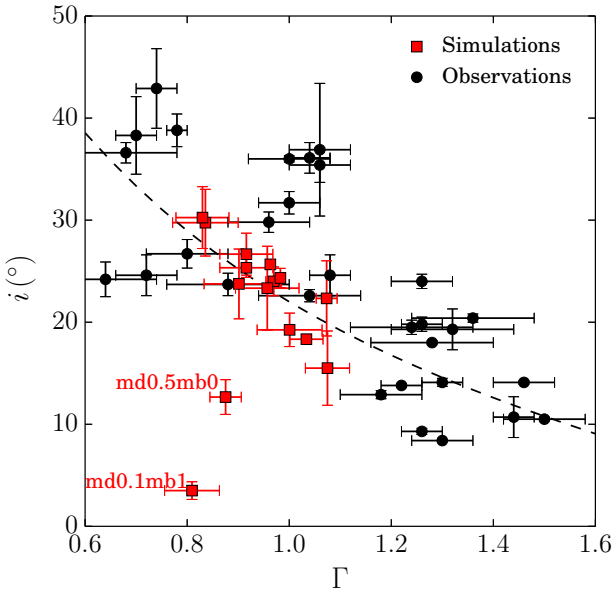

Figure 11. The relation between shear rate (Γ) and pitch angle (i) for the simulated galaxies shown in Table 4 (red squares) and observed galaxies (Seigar et al. 2006) (black circles). For simulated galaxies, the error bars on x-axis indicate the range of shear rates depending on the radius at which we measured the shear rates and pitch angles. The error bars on y-axis indicate the standard deviations of measured pitch angles at each radius. The black dashed curve indicates the result of Michikoshi & Kokubo (2014) given by equation (16).

total mass fraction ($f_{\rm f}$) and the shear rate (Γ) are important parameters that decide the disk galaxy morphology such as the number of spiral arms, pitch angle, and the formation of bars.

4 DISCUSSIONS

4.1 Hubble sequence and morphology

In previous sections, we saw that different initial conditions in our simulations lead to galaxies which from an observational perspective would be classified as being similar. Here we discuss the relation between the initial conditions, secular evolution, and the morphology of disk galaxies.

In Fig. 14 we present a subset of snapshots from our simulation on the Hubble sequence (Hubble 1926). In the Hubble sequence, the spirals are more loosely wound and the bulge is fainter from Sa to Sc. This is connected with the results we see in Section 3 where galaxies with a massive bulge have more tightly wound spiral arms due to the larger shear rate when the disk mass fraction is kept similar. Indeed, the sequence of spiral galaxies from Sa to Sc originates from changes in the initial distribution of the disk, bulge and dark matter halo.

Flocculent galaxies, which have patchy spiral arms, are realized by a model with a small disk to total mass fraction (see model md0.1mb1). Even after 10 Gyr this model did not form a bar and the data in Fig. 8 indicates that it will take more than a Hubble time before the bar forms.

Once the bar formation criteria is satisfied the spiral galaxies leave the spiral sequence and move into the SB sequence. If the barred galaxy started as a Sc galaxy then in the early stages it resembles the barred-spiral structures as seen in SBc galaxies. These galaxies then continue to evolve in SBb or SBa galaxies.

The barred-galaxy (SB) sequence is well understood, in particular when compared to the spiral sequence, using secular evolution. Once a bar develops and grows stronger it also becomes visible in the disk structure by the appearance of a ring. This ring-structure starts forming when the spiral arms become tightly wound, giving the galaxy the looks of an SBa galaxy, see for example Fig. A6).

The de Vaucouleurs classification (de Vaucouleurs 1959) appears when spiral galaxies evolve into barred galaxies. In the models where the disk is massive enough to form a bar, but less massive than the models md0.5mb1 and md1mb1Rd1.5, a ring structure appears after the bar has formed. In Fig. 3 and A7 we see that these models still retain some spiral structures in the outer parts of the disks. For models md1mb1 and md1.5mb5, which have a disk mass with $f_{\rm d} > 0.5$, a bar forms immediately after the start of the simulations (van Albada & Sancisi 1986; Binney & Tremaine 2008). They further show strong s-shaped structures and ring structures appear after the bar has fully developed (right most of Fig. 3). For these models we do not observe any spiral structure in the outer regions of the disk.

4.2 Grand-design spirals

As described in Section 3.3, swing amplification theory predicts that galaxies with massive disks (large disk-to-halo mass fraction) typically develop two spiral arms. This condition at the same time satisfies the constraints for the rapid formation of a bar. Both two-armed spirals and bars are structures of $m = 2$. In our models, galaxies with a massive disk often directly form a bar rather than first forming a

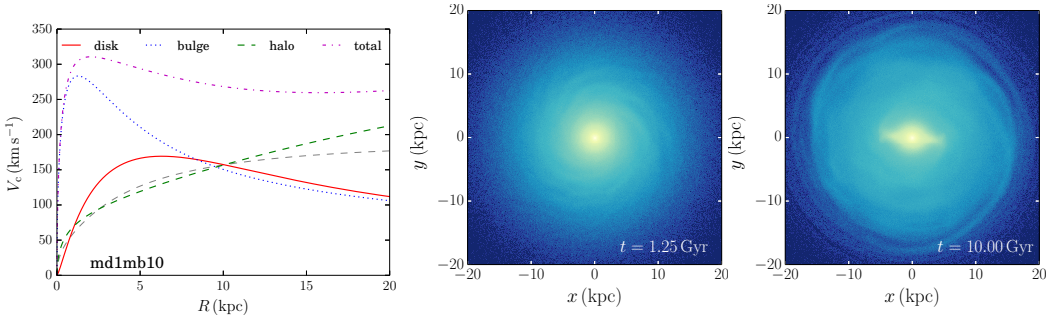

Figure 12. Snapshots for model md1mb10.

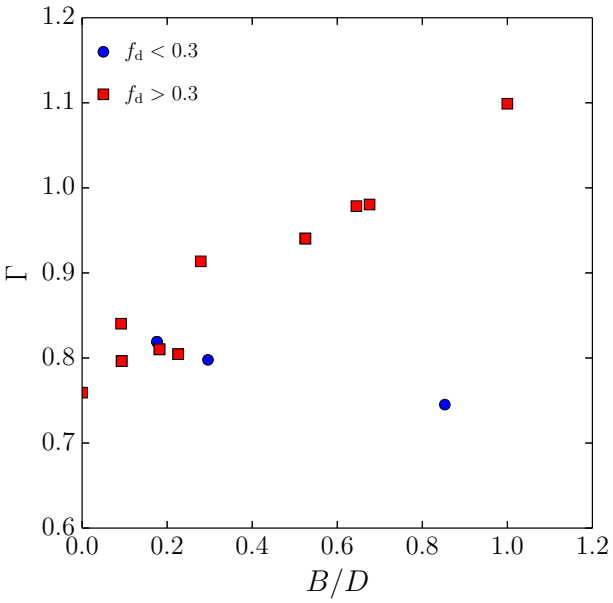

Figure 13. The relation between the shear rates at $2.2R_d$ and the bulge-to-disk mass ratio of our models. Circles and squares indicate models with $f_d(2.2R_d) < 0.3$ and $f_d(2.2R_d) > 0.3$, respectively.

two-armed spiral disk. This implies that $m = 2$ structures in galactic disks are mostly bars. However, from observations we know that two-armed grand-design spiral galaxies do actually exist. One possible cause is that perturbations induced by a companion galaxy leads to the formation of such a spiral galaxy. This was tested by Toomre & Toomre (1972) who, using simulations, showed that tidal interactions can lead to the formation of two spiral arms without a bar. If accompanying galaxies are indeed the driver for the formation of two armed spirals then the number of grand-design spirals with companions must exceed the number of isolated grand-design galaxies. Kormendy & Norman (1979) and Elmegreen & Elmegreen (1982) observationally showed that disk galaxies with companions consist of a larger fraction of grand-design spirals (0.6–1.0) compared to isolated galaxies (0.2–0.3). However, not all grand-design spiral galaxies have companions. M 74, for example, has no apparent companion (Kendall et al. 2011). In the following paragraphs we explore the formation of two-armed grand-design spirals without a companion.

In the previous sections we saw that a massive disks leads to $m = 2$ structures. On the other hand, a massive bulge suppresses the formation of a bar, but massive bulges tend to increase the number of spiral arms (e.g. model md1mb10). To create a grand-design spiral we therefore setup a new model, md1.5mb5, which has the largest disk mass-fraction of all our models ($f_d \sim 0.6$), and a moderately massive bulge, $B/D \sim 0.3$. This model is expected to form a bar. In Fig. 15 we present the initial rotation curve (left panel) and the density snapshots (right panels) for this model. At an age of $t = 1.25$ Gyr this model shows structure comparable to that observed in grand-design spirals, but only in the short time before the bar is formed. We conclude that grand-design spirals can form without companion, but that the structure is short-lived and disappears as soon as the bar forms.

Multi-arm spirals with a very small bulge (such as in M33) are considered to be transient structures just like grand-design spirals. Models md0.5mb0 and md1mb1Rd1.5 show multiple spiral arms and resemble M33 (see Fig. 3 and A7) shortly before the formation of a bar. Model md0.5mb0 has no bulge, a disk mass fraction of 0.38, and rotation curves with a similar shape as those of M33. Model

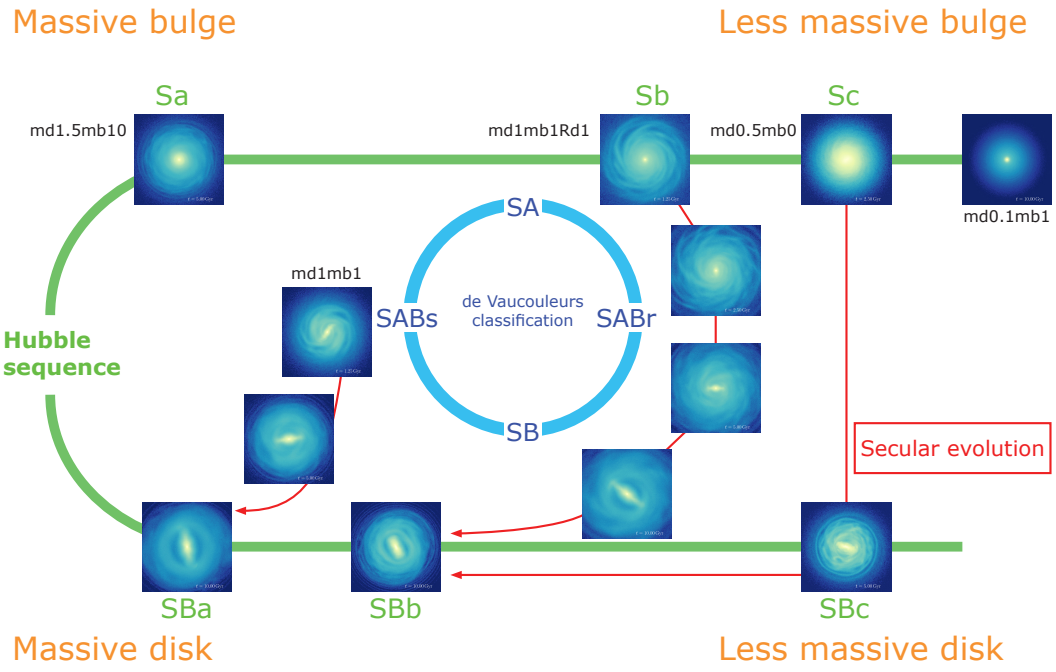

Figure 14. The Hubble sequence and de Vaucouleurs classification overlaid with snapshots of our models. The red arrows show the models secular evolution.

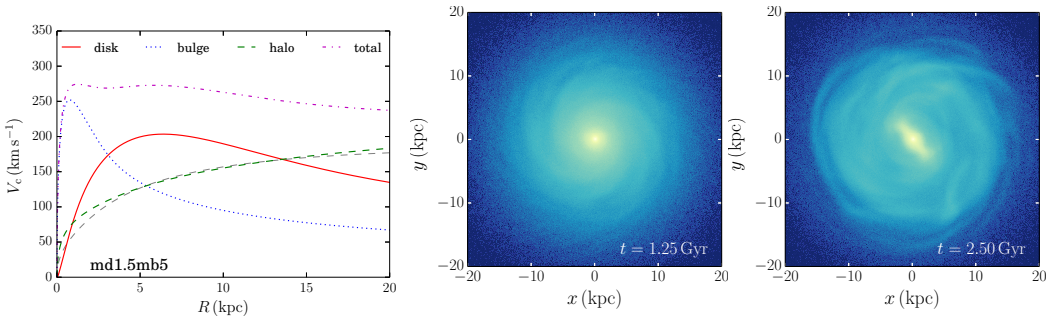

Figure 15. Initial rotation curves (left) and density snapshots for model md1.5mb5 at $t = 1.25$ Gyr (middle) and $t = 2.5$ Gyr (right).

md1mb1Rd1.5 has a bulge-to-disk mass ratio of ~ 0.1 and a disk mass fraction of 0.42. The observed bulge-to-disk mass ratio of M33 is smaller than 0.03 (Kormendy et al. 2010; Seigar 2011) and is considered to have a massive disk close to what is allowed by the mass maps (Corbelli et al. 2014). Near-infrared observations indicate that M33 is in the early stages of bar formation (Regan & Vogel 1994), which matches perfectly with our simulation, according to which M33-type disk galaxies eventually form a bar.

5 SUMMARY

We performed a series of galactic disk N-body simulations to investigate the formation and dynamical evolution of spiral arm and bar structures in stellar disks which are embedded in live dark matter halos. We adopted a range of initial conditions where the models have similar halo rotation curves, but different masses for the disk and bulge components, scale lengths, initial Q values, and halo spin parameters. The results indicate that the bar formation epoch increases exponentially as a function of the disk mass fraction with respect to the total mass at the reference radius (2.2 times the disk scale length), f_d. This relation is a consequence of swing amplification (Toomre 1981), which describes the amplification rate of the spiral arm when it transitions from leading arm to trailing arm because of the differential rotation of the disk. Swing amplification depends on the properties that characterize the disk, Toomre's Q and X parameters. When Q is fixed, the growth rate reaches its maximum when $1 < X < 2$. We computed X for $m = 2$ (X_2), which corresponds to a bar or two-armed spiral, for each of our models and found that this value is related to the bar's formation epoch.

The bar amplitude grows most efficiently when $1 < X_2 <$

2. For models with $1 < X_2 < 2$ the bar develops immediately after the start of the simulation. As X_2 increases beyond $X_2 = 2$, the growth rate decreases exponentially. We find that the bar formation epoch increases exponentially as X_2 increases beyond $X_2 = 2$, in other words f_d decreases.

Apart from X, the growth rate is also influenced by Q where a larger Q results in a slower growth. This indicates that the bar formation occurs later for larger values of Q. Our simulations confirm this and show that for the bar ($m = 2$) the growth rate is predicted by swing amplification and becomes visible when it grows beyond a certain amplitude.

Toomre's swing amplification theory further predicts that the number of spiral arms is related to the mass of the disk, with massive disks having fewer spiral arms. We confirmed this relation in our simulations.

The various initial conditions that we simulated resulted in a series of (barred) spiral galaxies similar to those that appear in the Hubble sequence. The fundamental subdivisions of spiral galaxies with massive bulges and tightly wound-up spiral arms from S(B)a to S(B)c can also be observed as a sequence in our simulations where the models with massive bulges have a larger shear rate.

We further found that Hubble's barred galaxy sequence is caused by the secular evolution of the bar. The barred-spiral galaxies initially start with wider spiral arms (larger pitch angle) just after the formation of the bar. Once the bar is formed it will start to heat up the disks outer parts, and the self-gravitating spiral arms disappear. Eventually, a ring-like structure forms around the bars. This secular evolution is consistent with the Hubble sequence from SBc to SBa. After the bars grow, we no longer see the clear spiral arms in the outer regions of the disks. This might imply that gas cooling and star formation is required in order to maintain the spiral arms in barred spiral galaxies for over a Hubble time (Schwarz 1981; Sellwood & Carlberg 1984).

In contrast, the Sa to Sc Hubble sequence relies on differences in the initial conditions and not on secular evolution. The opening angle of the spiral arms increases when the shear rate decreases. A larger shear rate can be realized when adopting a more centrally concentrated mass distribution, i.e. a more massive bulge. This is also seen in observations for which early spiral galaxies (Sc) tend to have a larger bulge-to-disk mass-ratio. If the other conditions are the same, less massive disks will have smaller shear rates and are therefore expected to have larger pitch angles. It is therefore difficult to explain the Hubble sequence with only the bulge-to-disk mass-ratio or the disk-to-halo mass-ratio. According to our results the disk-to-total mass fraction and shear rate are important parameters that determine the morphology of disk galaxies.

Our simulations further indicate that grand-design spirals are transient structures which immediately evolve into barred galaxies. Swing amplification teaches us that a massive disk is required to form two-armed spiral galaxies. This condition, at the same time, satisfies the short formation time of the bar structure. Grand-design spiral galaxies therefore must evolve into barred galaxies. We consider that isolated grand-design spiral galaxies are in the process of developing a bar.

ACKNOWLEDGMENTS

This work was supported by JSPS KAKENHI Grant Number 26800108 and the Netherlands Research School for Astronomy (NOVA). Simulations are performed using GPU clusters, HA-PACS at the University of Tsukuba, Piz Daint at CSCS and Little Green Machine II (621.016.701). Initial development has been done using the Titan computer Oak Ridge National Laboratory. This work was supported by a grant from the Swiss National Supercomputing Centre (CSCS) under project ID s548. This research used resources of the Oak Ridge Leadership Computing Facility at the Oak Ridge National Laboratory, which is supported by the Office of Science of the U.S. Department of Energy under Contract No. DE-AC05-00OR22725 and by the European Union's Horizon 2020 research and innovation programme under grant agreement No 671564 (COMPAT project).

APPENDIX A: THE EFFECTS OF OTHER PARAMETERS

We discussed the effect of the bulge and disk masses on the development of bars and spiral arms in the main text. Here we briefly summarize the effects of the other parameters we investigated.

A1 Halo spin

The spin of the halo is known to be an important parameter that affects the bar's secular evolution. Long et al. (2014) showed that a co-rotating disk and halo speed up of the bar formation, but decrease its final length. This is due to the angular momentum transfer between the disk and halo. If the halo does not spin it absorbs the bar's angular momentum, which slows down the bar and increases its length. A co-rotating halo, however, returns angular momentum to the disk instead of just absorbing it. This stabilizes the angular momentum transfer, and the bar evolution ceases.

We setup a few models, based on model md1mb1, but now with a rotating halo. In order to give spin to the halo we change the sign of the angular momentum z component, L_z. For models md1mb1s0.65 and md1mb1s0.8, 65 and 85 % of the halo particles are rotating in the same direction as the disk. For models without rotation, this value is 50 %.

To compare our results with previous studies, we measure the spin parameter Peebles (1969, 1971):

$$\lambda = \frac{J|E|^{1/2}}{GM_\mathrm{h}^{5/2}}, \tag{A1}$$

where J is the magnitude of the angular momentum vector, E is the total energy. In our models, $\alpha_\mathrm{h} = 0.65$ (0.8) correspond to $\lambda \sim 0.03$ (0.06).

In Fig. A1 we present the effect the halo spin has on models md1mb1s0.65 and md1mb1s0.8. The results indicate that the halo spin affects the bar length, since for the models with spin it is shorter than for the same model without spin (md1mb1s).

In Fig. A2 we show the length and maximum amplitude of the resulting bars. In contrast to the results of Saha & Naab (2013) and Long et al. (2014) the bar formation

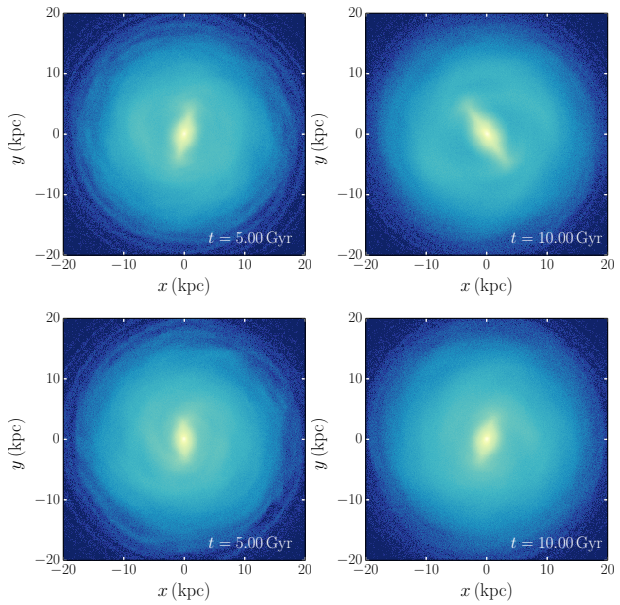

Figure A1. Snapshots for models md1mb1s0.65 (top) and md1mb1s0.8 (bottom), which are the same as model md1mb1 (Fig. 2 and 3, far most right panels) but with halo spins.

epochs of our models are very similar, although a faster bar formation was expected when using a larger halo spin.

In addition to the bar forming models above, we also added halo spin to a model that shows no bar formation within 10 Gyr. This model, md0.5Rd1.5s, is based on md0.5Rd1.5 but now with a halo spin of 0.8. In Fig. A3, we present the snapshots of the above models at $t = 10$ Gyr. In contrast to the barred galaxies, their spiral structures look quite similar. To quantitatively compare the spiral amplitudes we use the total amplitude of the spiral arms given by $\sum_{m=1}^{10} |A_m|^2$, where A_m is the Fourier amplitude (Eq. 10). Instead of the bar amplitude, we measured the spirals total amplitude at $2.2R_\mathrm{d}$ and at $1.1R_\mathrm{d}$ (for this model 9.5 and 4.5 kpc, respectively), the results are shown in Fig. A4. The evolution of the spiral amplitudes are quite similar for both models. This suggest that the angular momentum transfer between the disk and halo is not efficient for spiral arms.

A2 Initial Q value

To verify the expectation that the initial value of Toomre's Q parameter (Q_0) influences the bar and spiral structure, we created a set of models in which we varied this parameter.

The models are based on md0.5mb0, with one having an initially unstable disk (md0.5mb0Q0.5) and the other having a large Q_0, in which no spiral arms develop (md0.5mb0Q2.0). The time evolution of the bar's amplitude and length is presented in Fig. A5 and the density snapshots are shown in Fig. A6. For md0.5mb0Q2.0 there is no sign of spiral or bar structure until ~ 5 Gyr, but a bar develops shortly after that (left panel of Fig. A5). This matches with the expectation that Q_0 influences the bar formation epoch, the smaller the Q_0 value the faster the bar forms. We also confirmed that the final bar length does not depend on Q_0.

This further proves (as discussed in Section 3.3) that the growth rate of swing amplification governs the bar formation timescale. The growth rate decreases as Q increases (Toomre 1981) which is confirmed by our simulations. With $Q_0 = 2.0$, the disk is initially stable and hence the spiral structure has to be induced by the bar. These ring-like spiral arms are sometimes seen in SB0–SBa galaxies such as NGC 5101 (Ho et al. 2011).

A3 Disk scale length

We further examine models md1mb1Rd1.5 and md0.5mb1Rd1.5, which have a larger disk length scale. For these models the total disk mass is the same as that of models md1mb1 and md0.5mb1, but the disk scale length is larger. The changed disk scale length results in different rotation curves (see Fig. A7). Given Eq. 9 we expect that this leads to fewer spiral arms. The top views of these models are presented in Fig. A7 (right panels) and the evolution of the bar's amplitude and length in Fig. A8. The bar formation epoch of model md1mb1Rd1.5 (2 Gyr) is later than that of model mdmb1 (1 Gyr). Model md0.5mb1Rd1.5 did not form a bar within 10 Gyr, although model md0.5mb1 formed a bar at ~ 6 Gyr. The difference between these models is that the disk mass fraction (f_d) for model md1mb1R1.5 and md0.5mb1R1.5 is smaller than those for model md1mb1 and md0.5mb1 (see Table 3). Although the bar formation starts later for model md1mb1Rd1.5, the bar grows faster, and the final bar length at 10 Gyr is comparable for these models. The bar's secular evolution, however, may continue further. In order to understand what decides the final bar length further simulations are required.

APPENDIX B: EVOLUTION OF SPIRAL ARMS IN A LIVE HALO

For the formation and evolution of bars, the effect of a live halo has been investigated in previous work, and it has been shown that the angular-momentum transfer from bars to live halos helps the growth of bars (Debattista & Sellwood 2000; Athanassoula 2002). Previous work, however, focused on the evolution of bars but not on spiral arms. In most of the previous work rigid halo simulations were used to study the dynamical evolution of spiral arms. As all our simulations are performed using a live halo, we made a comparison to the results in Fujii et al. (2011) to test the effect of a live halo on the spiral structure.

In Fig. B1 the relation between Q and the total amplitude ($\sum_{m=1}^{20} |A_m|^2$) at $t = 0, 0.125, 2.5, 5$, and 10 Gyr is presented for our models at $R = 2.2R_\mathrm{d}$. The left panel shows the models which did not form a bar until 10 Gyr. In Fujii et al. (2011) we found that the spiral amplitudes grow up to a maximum given by the following equation:

$$A_m = 3.5C - 1.0 - 0.75Q^2, \qquad \text{(B1)}$$

where C depends on the shape of the spiral arms, for a homogeneous sphere $C = 3/5$. If we consider that $|A_m|^2$ is similar to the total amplitude, then the amplitudes of self-gravitating spiral arms can be analytically obtained as a function of Q. Fujii et al. (2011) further found that after the spiral arm has reached its maximum amplitude, Q increases because of the heating of the spiral arms and, following equation B1, the amplitude starts to decay (black curve in Fig. B1). For

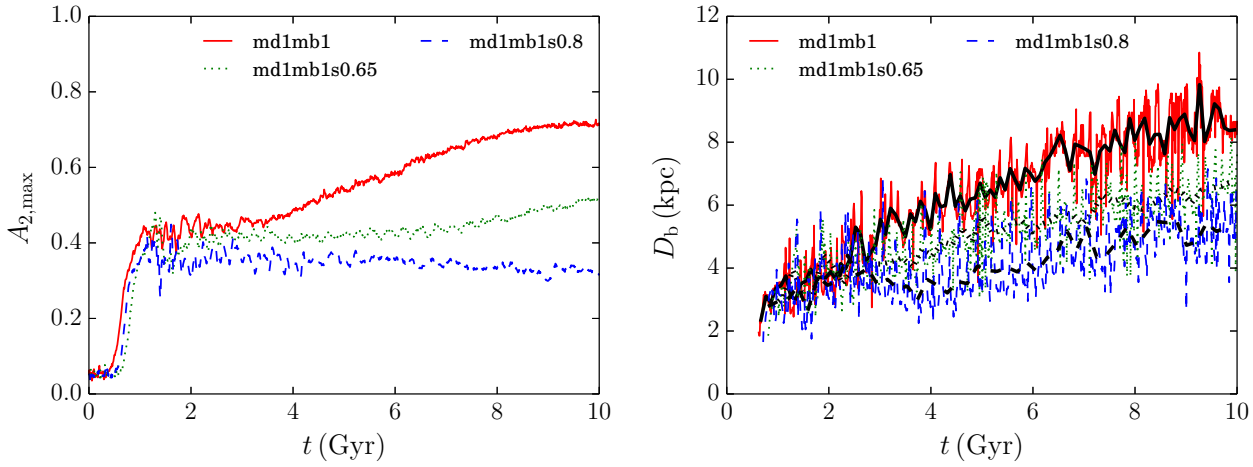

Figure A2. Same as Fig. 7, but for models md1mb1, md1mb1s0.65, and md1mb1s0.8.

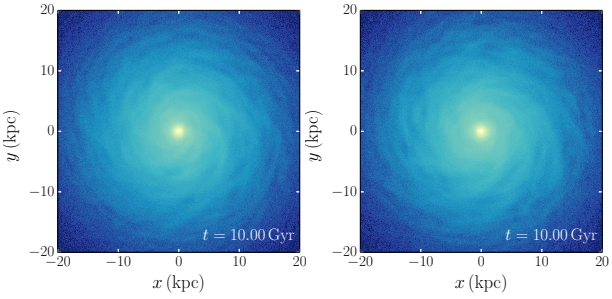

Figure A3. Snapshots for models md0.5Rd1.5 (left) and md0.5Rd1.5s (right).

models without a bar we obtain the same results as for our models with live halos, although most of the data points are from before the amplitude decrease (see the left panel of Fig. B1). Results for bar forming models are shown in the right panel of Fig. B1. After the bar forms, the developed amplitudes exceed that of the maximum given by Q, this is indicated by the larger symbols in the figures. The symbols are clearly above the theoretical line and Q keeps increasing due to the bar induced heating.

Snapshots of the bar models indicate that in the disks outer regions the spiral structure disappears, however the Fourier amplitudes are still larger than those for the models without bars. The amplitude tends to decrease as Q increases, except for models md1mb1, md1Rd1.5, and md0.5mb0, where the bar length reaches the reference radius by 10 Gyr. In these models, we take the bar's amplitude as the total amplitude.

The distribution of Q as a function of the galactic radius for models md1mb1 (strong bar) and md0.5mb4 (without bar, although a bar forms after 10 Gyr) is presented in Fig. B2. The spiral arms heat up the disk moderately (left panel), but the bars heat up the disk dramatically once they are formed (right panel).

Another effect of the bar is that it seems to prevent the formation of self-gravitating spiral arms, which corresponds to the number of spiral arms expected from swing amplification. In Fig. B3, the expected number of spiral arms (m_X) for model md1mb1 at $t = 1.25$, 2.5, 5, and 10 Gyr is presented. In the outer regions of the disk, m_X decreases as the bar develops, but still $m_X > 2$. However, there are corresponding spiral arms (see snapshots of md1mb1 in Fig. 3). One possible reason for this is that the high Q value prevents the formation of self-gravitating spiral arms after the bar has formed.

To conclude, using a live halo instead of an analytic halo is important when one is studying the bar itself and bar formation properties in disk galaxies. Since the live halo will influence the angular momentum of the bar its speed and length will be different from when using an analytic halo. The effect on spiral structure without a bar, however, is not so pronounced.

REFERENCES

Athanassoula E., 2002, ApJ, 569, L83
Baba J., 2015, MNRAS, 454, 2954
Baba J., Saitoh T. R., Wada K., 2013, ApJ, 763, 46
Barazza F. D., Jogee S., Marinova I., 2008, ApJ, 675, 1194
Barnes J., Hut P., 1986, Nature, 324, 446
Bédorf J., Gaburov E., Portegies Zwart S., 2012, Journal of Computational Physics, 231, 2825
Bédorf J., Gaburov E., Fujii M. S., Nitadori K., Ishiyama T., Portegies Zwart S., 2014, in Proceedings of the International Conference for High Performance Computing, Networking, Storage and Analysis, p. 54-65. pp 54–65 (arXiv:1412.0659), doi:10.1109/SC.2014.10OTHER: http://dl.acm.org/citation.cfm?id=2683600
Binney J., Tremaine S., 2008, Galactic Dynamics: Second Edition. Princeton University Press
Bottema R., 2003, MNRAS, 344, 358
Carlberg R. G., Freedman W. L., 1985, ApJ, 298, 486
Combes F., Debbasch F., Friedli D., Pfenniger D., 1990, A&A, 233, 82
Corbelli E., Thilker D., Zibetti S., Giovanardi C., Salucci P., 2014, A&A, 572, A23
D'Onghia E., 2015, ApJ, 808, L8
Debattista V. P., Sellwood J. A., 2000, ApJ, 543, 704
Dobbs C., Baba J., 2014, PASA, 31, 35
Dubinski J., Berentzen I., Shlosman I., 2009, ApJ, 697, 293
Efstathiou G., Lake G., Negroponte J., 1982, MNRAS, 199, 1069
Elmegreen D. M., Elmegreen B. G., 1982, MNRAS, 201, 1021

[htbp]

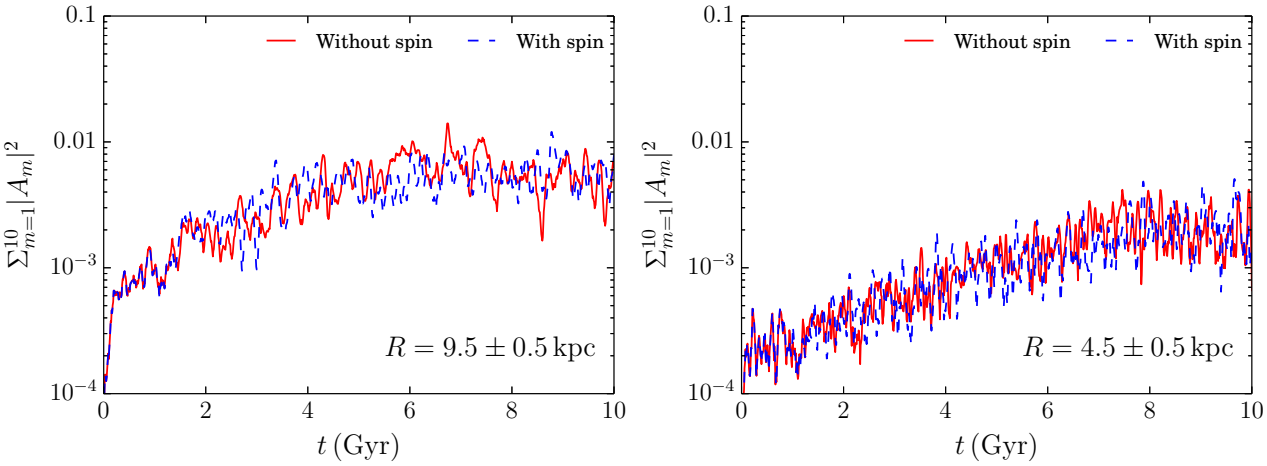

Figure A4. Total power for models md0.5Rd1.5 and md0.5Rd1.5s at $R = 9.5$ kpc (left) and 4.5 kpc (right).

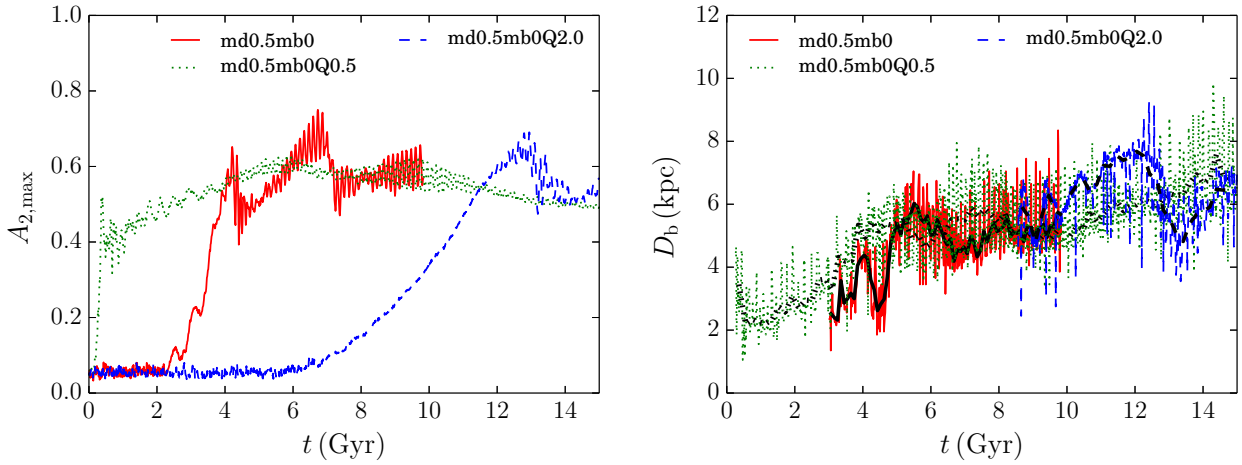

Figure A5. Same as Fig. 7, but for models md0.5mb0Q0.5 and md0.5mb0Q2.0.

Fujii M. S., Baba J., Saitoh T. R., Makino J., Kokubo E., Wada K., 2011, ApJ, 730, 109
Goldreich P., Lynden-Bell D., 1965, MNRAS, 130, 125
Grand R. J. J., Kawata D., Cropper M., 2013, A&A, 553, A77
Hernquist L., 1990, ApJ, 356, 359
Ho L. C., Li Z.-Y., Barth A. J., Seigar M. S., Peng C. Y., 2011, ApJS, 197, 21
Hohl F., 1971, ApJ, 168, 343
Hubble E. P., 1926, ApJ, 64, 321
Iannuzzi F., Athanassoula E., 2013, MNRAS, 436, 1161
Julian W. H., Toomre A., 1966, ApJ, 146, 810
Kendall S., Kennicutt R. C., Clarke C., 2011, MNRAS, 414, 538
Kormendy J., Norman C. A., 1979, ApJ, 233, 539
Kormendy J., Drory N., Bender R., Cornell M. E., 2010, ApJ, 723, 54
Kunder A., et al., 2012, AJ, 143, 57
Lin C. C., Shu F. H., 1964, ApJ, 140, 646
Long S., Shlosman I., Heller C., 2014, ApJ, 783, L18
Michikoshi S., Kokubo E., 2014, ApJ, 787, 174
Michikoshi S., Kokubo E., 2016a, ApJ, 821, 35
Michikoshi S., Kokubo E., 2016b, ApJ, 823, 121
Navarro J. F., Frenk C. S., White S. D. M., 1997, ApJ, 490, 493
Okamoto T., Isoe M., Habe A., 2015, PASJ, 67, 63
Ostriker J. P., Peebles P. J. E., 1973, ApJ, 186, 467
Peebles P. J. E., 1969, ApJ, 155, 393
Peebles P. J. E., 1971, A&A, 11, 377
Portegies Zwart S., Bédorf J., 2015, Computer, 48, 50
Regan M. W., Vogel S. N., 1994, ApJ, 434, 536
Saha K., Naab T., 2013, MNRAS, 434, 1287
Scannapieco C., Athanassoula E., 2012, MNRAS, 425, L10
Schwarz M. P., 1981, ApJ, 247, 77
Seigar M. S., 2005, MNRAS, 361, L20
Seigar M. S., 2011, ISRN Astronomy and Astrophysics, 2011, 4
Seigar M. S., Bullock J. S., Barth A. J., Ho L. C., 2006, ApJ, 645, 1012
Sellwood J. A., Carlberg R. G., 1984, ApJ, 282, 61
Sellwood J. A., Carlberg R. G., 2014, ApJ, 785, 137
Sellwood J. A., Evans N. W., 2001, ApJ, 546, 176
Shen J., Rich R. M., Kormendy J., Howard C. D., De Propris R., Kunder A., 2010, ApJ, 720, L72
Tempel E., Tenjes P., 2006, MNRAS, 371, 1269
Toomre A., 1964, ApJ, 139, 1217
Toomre A., 1981, in Fall S. M., Lynden-Bell D., eds, Structure and Evolution of Normal Galaxies. pp 111–136
Toomre A., Toomre J., 1972, ApJ, 178, 623
Widrow L. M., Dubinski J., 2005, ApJ, 631, 838
Widrow L. M., Pym B., Dubinski J., 2008, ApJ, 679, 1239
Zasov A. V., Moiseev A. V., Khoperskov A. V., Sidorova E. A.,

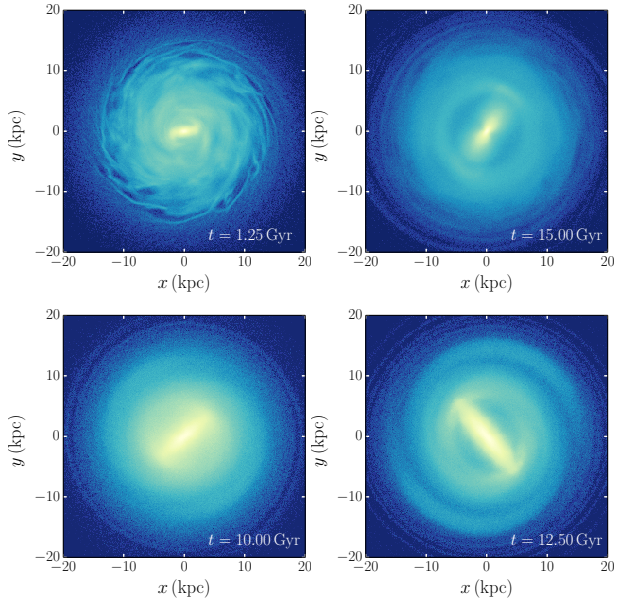

Figure A6. Snapshots for models md0.5mb0Q0.5 (top) and md0.5mb0Q2.0 (bottom).

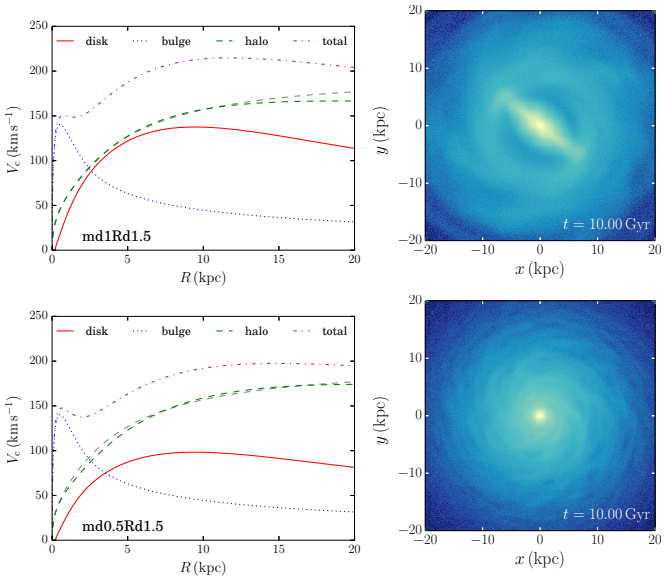

Figure A7. Rotation curves (left) and snapshots at 10 Gyr (right) for models md1mb1Rd1.5 (top) and md0.5mb1Rd1.5 (bottom).

2008, Astronomy Reports, 52, 79
de Vaucouleurs G., 1959, Handbuch der Physik, 53, 275
van Albada T. S., Sancisi R., 1986, Philosophical Transactions of the Royal Society of London Series A, 320, 447

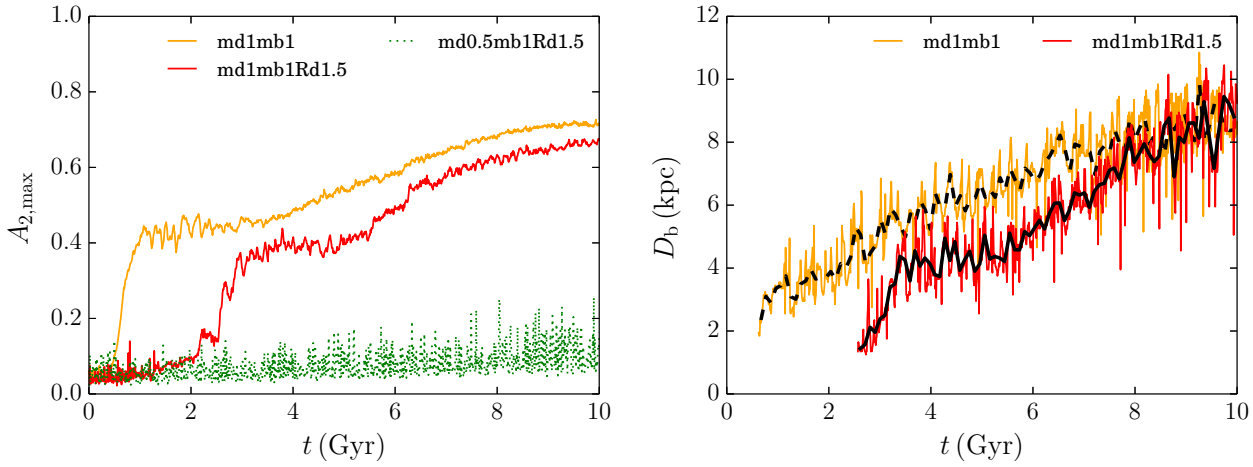

Figure A8. Same as Fig. 7, but now for models md1mb1Rd1.5 and md0.5mb1Rd1.5 with md1mb1 shown as reference.

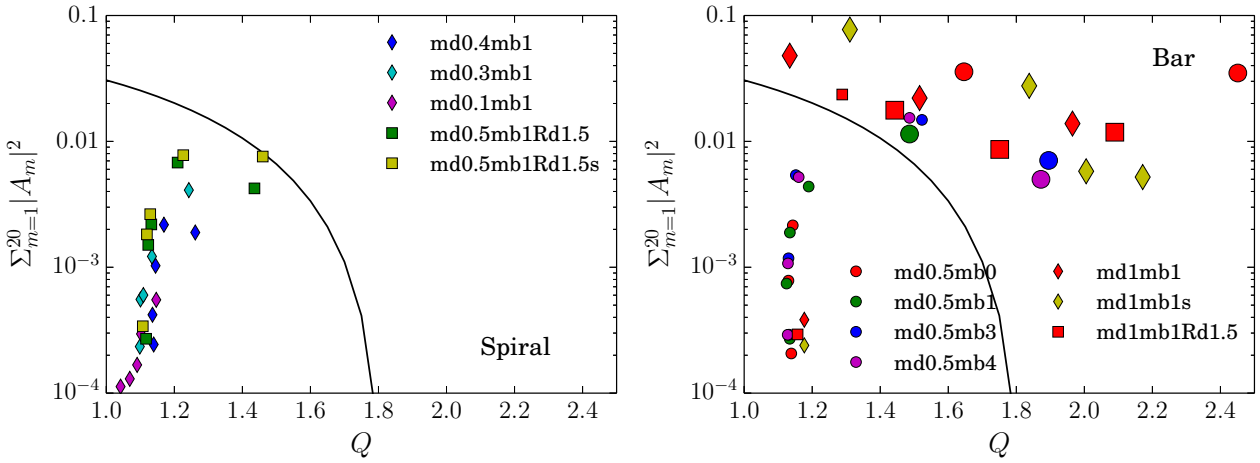

Figure B1. Relation between Q and the total power of the Fourier amplitudes at the reference radii ($R = 6.5 \pm 0.5$ kpc, except for models md1Rd1.5, md0.5Rd1.5, md0.5Rd1.5s where $R = 9.5 \pm 0.5$ kpc) at $t = 0, 0.125, 2.5, 5$, and 10 Gyr. Large symbols indicate the data points after the bar formation. The total power is averaged over 20 snapshots (~ 20 Myr). Black curves indicate $|0.1A_{\rm m}|^2$ using Eq. B1.

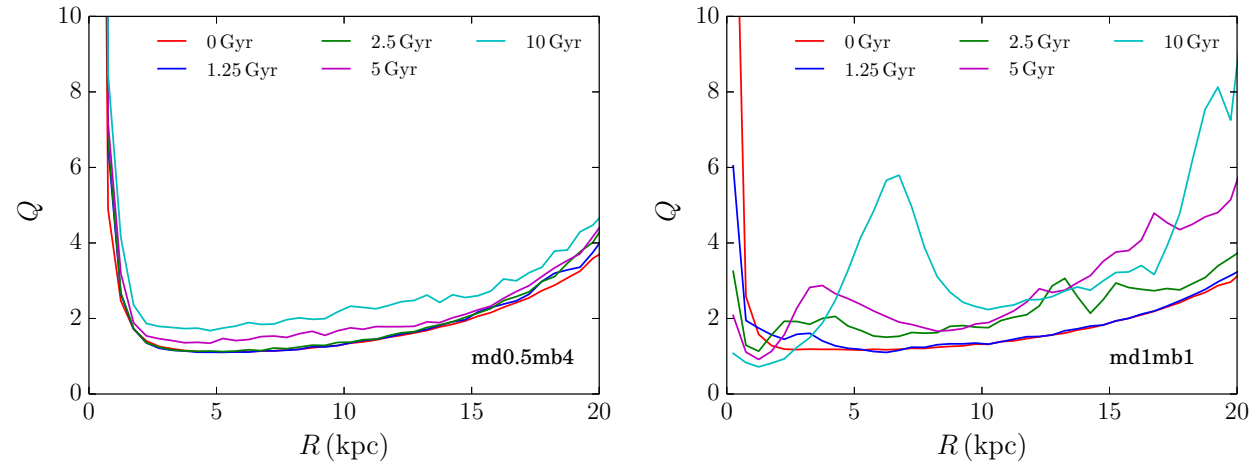

Figure B2. Time evolution of Toomre's Q for models md0.5mb4 (left) and md1mb1 (right). The peak in the cyan curve at $R \sim 7$kpc corresponds to the end of the bar.

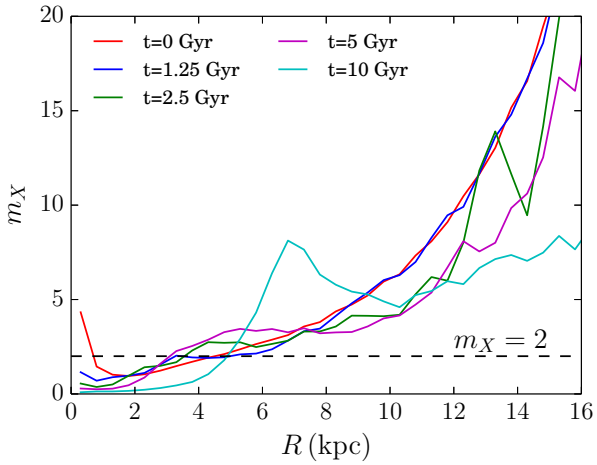

Figure B3. The number of spiral arms using Eq. 9 at $t = 0$, 0.125, 0.25, 5, and 10 Gyr for model md1mb1. The peak in the cyan curve at $R \sim 7$ kpc corresponds to the bar end.